Transient demyelination causes long-term cognitive impairment, myelin alteration and network synchrony defects

Océane Mercier, Pascale P Quilichini, Karine Magalon, Florian Gil, Antoine Ghestem, Fabrice Richard, Thomas Boudier, Myriam Cayre, Pascale Durbec

Received: 17 May 2023 | Revised: 26 January 2024 | Accepted: 5 February 2024

DOI: 10.1002/glia.24513

GLIA

WILEY

RESEARCH ARTICLE

Transient demyelination causes long-term cognitive impairment, myelin alteration and network synchrony defects

Océane Mercier[1] | Pascale P. Quilichini[2] | Karine Magalon[1] | Florian Gil[1] | Antoine Ghestem[2] | Fabrice Richard[1] | Thomas Boudier[3] | Myriam Cayre[1] | Pascale Durbec[1]

[1]UMR7288 after IBDM, Aix Marseille Univ, CNRS, IBDM, Marseille, France

[2]U1106 after INS, Aix Marseille Univ, INSERM, INS, Inst Neurosci Syst, Marseille, France

[3]Aix Marseille Univ, Turing Centre for Living Systems, Marseille, France

Correspondence
Pascale Durbec, IBDM-UMR 7288, Case 907, Parc Scientifique de Luminy, 13288 Marseille Cedex 09, France.
Email: pascale.durbec@univ-amu.fr

Funding information
Agence Nationale de la Recherche, Grant/Award Numbers: ANR-10-INSB-04-01, ANR-17-EURE-0029; Aix-Marseille Université; Centre National de la Recherche Scientifique

Abstract

In the adult brain, activity-dependent myelin plasticity is required for proper learning and memory consolidation. Myelin loss, alteration, or even subtle structural modifications can therefore compromise the network activity, leading to functional impairment. In multiple sclerosis, spontaneous myelin repair process is possible, but it is heterogeneous among patients, sometimes leading to functional recovery, often more visible at the motor level than at the cognitive level. In cuprizone-treated mouse model, massive brain demyelination is followed by spontaneous and robust remyelination. However, reformed myelin, although functional, may not exhibit the same morphological characteristics as developmental myelin, which can have an impact on the activity of neural networks. In this context, we used the cuprizone-treated mouse model to analyze the structural, functional, and cognitive long-term effects of transient demyelination. Our results show that an episode of demyelination induces despite remyelination long-term cognitive impairment, such as deficits in spatial working memory, social memory, cognitive flexibility, and hyperactivity. These deficits were associated with a reduction in myelin content in the medial prefrontal cortex (mPFC) and hippocampus (HPC), as well as structural myelin modifications, suggesting that the remyelination process may be imperfect in these structures. In vivo electrophysiological recordings showed that the demyelination episode altered the synchronization of HPC-mPFC activity, which is crucial for memory processes. Altogether, our data indicate that the myelin repair process following transient demyelination does not allow the complete recovery of the initial myelin properties in cortical structures. These subtle modifications alter network features, leading to prolonged cognitive deficits in mice.

KEYWORDS
Myelin regeneration, Cognition, Network activity, Mouse model of multiple sclerosis

1 | INTRODUCTION

In the CNS, oligodendrocyte-generated myelin plays crucial roles in action potential propagation and metabolic support to neurons. Myelin formation, which occurs postnatally through terminal differentiation of oligodendrocyte progenitor cells (OPCs), is maintained throughout life. In adults, myelin formation and remodeling are modulated by neuronal activity in response to environmental, sensorimotor,

social, and cognitive factors (Gibson et al., 2014; Kato & Wake, 2021). New myelin can influence action potential conduction velocity (Cullen et al., 2021) and fine-tune neuronal network activity (Chorghay et al., 2018). This plasticity is required for learning, memory consolidation, and recall (McKenzie et al., 2014; Pan et al., 2020; Steadman et al., 2020).

Activity-dependent myelin plasticity occurs in various forms. OPCs from the reservoir in the adult brain can differentiate into oligodendrocytes (Dawson, 2003; Dimou et al., 2008; Rivers et al., 2008), and preexisting mature oligodendrocytes can create new sheaths (Bacmeister et al., 2020). The myelin structure undergoes subtle activity-modulated modifications (Etxeberria et al., 2016; Jeffries et al., 2016; Xin & Chan, 2020; Young et al., 2013) regarding myelin thickness and the size and number of internodes and nodes of Ranvier, which are necessary for rapid and efficient action potential propagation. Recent data demonstrated that learning can modulate the length of nodes of Ranvier without affecting internode number and size in the corpus callosum (CC) and motor cortex (Cullen et al., 2021).

Myelin loss, alteration, or even subtle structural modifications can compromise network activity, resulting in mild impairment to profound disability, such as in multiple sclerosis (MS). MS, the main demyelinating disorder in humans, is an autoimmune disease, in which inflammation triggers myelin destruction and, ultimately, neuronal degeneration, leading to sensorimotor impairment. The cognitive impact is rarely addressed despite being present as cognitive impairment altering memory, attention, or executive function in half of MS patients (Chiaravalloti & DeLuca, 2008). In rodents, cuprizone-induced demyelination leads to reproducible motor and coordination problems (Sen et al., 2019), as well as deficits in memory, learning, or social interaction (Sen et al., 2019).

Self-repair process in MS patients, potentially restoring myelin and function, were important discoveries. Although mainly described for motor deficits, demyelinating lesions are also found in cortical gray matter, correlating with physical and cognitive disabilities, including memory loss (Calabrese et al., 2013), but much less is known about myelin repair capacity in cortical circuits as in vivo remyelination studies focused on the white matter. Although myelin repair is unpredictable in humans, it is robust following massive demyelination in cuprizone-treated rodent models. This spontaneous remyelination is supported by the mobilization of OPCs present in gray and white matter (Dimou et al., 2008; Young et al., 2013; Zawadzka et al., 2010) and involves subventricular zone-derived progenitors contributing to myelin repair in the CC (Brousse et al., 2015; El Waly et al., 2018; Xing et al., 2014).

Although functional, morphological characteristics differ between reformed and constitutive myelin, as exemplified by shorter and thinner myelin sheaths and higher number of nodes of Ranvier in the CC after remyelination (Pfeiffer et al., 2019; Young et al., 2013). Myelin regeneration is slower in gray matter, and myelin patterns are altered after cortical remyelination (Bacmeister et al., 2020; Orthmann-Murphy et al., 2020). As small changes in myelin thickness or nodal structures may have a major functional impact on neural network activities (Pajevic et al., 2014), efficient remyelination not necessarily implies efficient functional outcomes. In the cuprizone model, robust remyelination follows extensive demyelination. Although most motor deficits are restored once remyelination is complete, some persist (Franco-Pons et al., 2007; Tomas-Roig et al., 2019) or even re-appear (Manrique-Hoyos et al., 2012). The long-term evolution of cognitive function after demyelination/remyelination episodes has not been thoroughly investigated.

Here, we used the cuprizone model to assess behavioral outcomes of demyelination/remyelination processes, focusing on cognitive functions, and analyzed the features of newly formed myelin in gray matter regions associated with these functions. Our results demonstrated long-term impairment of specific cognitive functions despite remyelination, including spatial working memory, short-term social memory, cognitive flexibility, and exploratory hyperactivity. These deficits were associated with incomplete recovery of myelin content and structure in the medial prefrontal cortex (mPFC) and hippocampus (HPC), two cortical structures involved in cognition. In vivo electrophysiological recordings showed that HPC-mPFC synchronization, which is crucial for memory consolidation, was altered during the demyelination episode and not restored after remyelination. Overall, our data revealed prolonged cognitive deficits in cuprizone-treated mice associated with subtle myelin modifications and altered network features in related brain areas.

2 | MATERIALS AND METHODS

2.1 | Animals

All animal-related procedures were performed in accordance with the guidelines by the French Ministry of Agriculture (Animal Rights Division) and have been approved by the "Direction Départementale des Services Vétérinaires" and the Ethics Committee (ID numbers F1305521 for animal house and #21963-2019091112003475 and #32172-2021062910481440-v4 for research projects). Mice were housed under standard conditions and maintained on a 12 h/12 h light/dark cycle with ad libitum access to food and water. All efforts were made to minimize the number of animals used. Male 8-week-old C57BL/6 mice (Janvier lab) were used for all experiments after a one-week acclimatization period except oligodendrocyte lineage tracing where heterozygous Cre mice were crossed with homozygous mTmG reporters (Muzumdar et al., 2007) to generate double-heterozygous *Plp-Cre^{ERT2}:mTmG* mice. *Plp-Cre^{ERT2}:mTmG* mice (males and females) were induced with a single oral dose of 50 mg/kg tamoxifen 24 h before sacrifice.

2.2 | Demyelination induction

Age-matched C57BL/6 mice were randomly allocated to either the control (CTL) or cuprizone (CUP) group. To induce demyelination, 0.2% cuprizone (Sigma) was administered with food for 5 weeks and changed every day. Mice were sacrificed at three time points: (i) at

the demyelination peak, after 5 weeks of cuprizone treatment (W5); (ii) after short-term remyelination, 6 weeks after cuprizone removal (W11); and (iii) after long-term remyelination, 5 months after cuprizone removal (W26).

2.3 | Electrophysiological recordings

Animals (12 adult male C57BL/6 mice) were anesthetized with i.p. ketamine/xylazine (100 and 10 mg/kg, Renaudin Cip:34009 57854195 and CENTRAVET Cat#ROM001, respectively) with additional doses every 2 h during electrophysiological recordings. The animal was placed in a stereotaxic frame (Kopf #962, Phymep) and received a local subcutaneous ropivacaine injection (2 mg/kg). After exposing the skull, two stainless-steel screws (00–90) were implanted above the cerebellum as reference and ground electrodes. Two craniotomies targeted the CA1 HPC (bregma AP −2.7 mm, ML −2.7 mm, DV −1.2 mm, 20° angle) and the prelimbic mPFC area (bregma AP +1.7 mm, ML −0.3 mm, DV −1.5 mm). HPC and mPFC activities were simultaneously recorded using 64-site and 32-site E probes (Cambridge Neurotech), respectively (Supplementary Figure S4A).

Both probes mounted on individual stereotaxic manipulators were independently lowered using motorized descenders (IVM, Scientifica). The HPC probe positioning was confirmed using the presence of unit activity in cell body layers and ripples (120–200 Hz) in the stratum pyramidale, and the mPFC probe position was adjusted according to the presence of unit activity at ±100 µm of the DV coordinate.

Extracellular signals were amplified (1000×), bandpass-filtered (1–5000 Hz), and acquired continuously at 30 kHz using an acquisition board (v2.4, Open Ephys) at 16-bit resolution. Raw data were pre-processed using NEUROSUITE (https://neurosuite.sourceforge.net/; RRID: SCR_008020) (Hazan et al., 2006). The signal was downsampled to 1250 Hz for local field potential (LFP) analysis. Slow oscillation (SO) periods were identified, and visually selected epochs were confirmed using whitened power ratios in the SO band (0.5–2 Hz) in the mPFC and neighboring bands (1–3 and 7–14 Hz) of the CA1 pyramidal layer, in conjunction with visual raw trace inspection (Quilichini et al., 2010).

After recording, the animals were injected with a lethal pentobarbital sodium dose (150 mg/kg, i.p.) and perfused intracardially with 4% paraformaldehyde/0.12 M PBS, pH 7.4. The brains were removed and post-fixed at 4°C overnight. They were then rinsed in PBS, incubated in a 20% sucrose/PBS for 24 h, embedded in Cryomatrix (Shandon, ThermoFisher), and frozen at −80°C with dry ice. The frozen brain was then sliced into 40-µm-thick coronal sections using a cryostat. Electrode positions were confirmed by detecting DiIC18 (3) (Interchim) applied via the electrodes and Nissl staining (NeuroTrace 500/5225 Green Fluorescent Nissl Stain; Invitrogen) (Supplementary Figure S4B). Only experiments with appropriate electrode positions were used for analyses.

Spectral analyses on prewhitened LFPs used a modified multitaper FFT MATLAB package (Ferraris et al., 2018; Mitra & Pesaran, 1999), the Chronux toolbox (http://chronux.org/), the FMA Toolbox (Maingret et al., 2016) and custom-written MATLAB scripts (RRID: SCR_001622 and RRID: SCR_008020). The parameters were an FFT window size of 4 s, 3–5 tapers, 0.15-Hz frequency bins, nonoverlapping successive windows, and time bandwidth of 3 (Mitra & Pesaran, 1999; Quilichini et al., 2010). SO periods had a minimum duration of 30 min. We used the previously defined "comodugram" analysis (Ferraris et al., 2018; Quilichini et al., 2010) to assess the power-power correlation of HPC and mPFC LFPs for each frequency pair between 1 and 200 Hz using the abovementioned FFT parameters. The correlation coefficients between normalized spectral power values were calculated with the "corrcoef.m" MATLAB function. The sharp wave-ripple (SPW-R) detection in stratum pyramidale LFPs was described previously (Ferraris et al., 2018). SPW-Rs were detected during SO periods, which were digitally band-pass-filtered (100–250 Hz), squared, low-pass-filtered (8.8 ms running average), and normalized, yielding a transformed signal R(t). SPW-Rs were defined as events exceeding 5 with R(t) remaining >2 for 30–100 ms. To compute SPW-R SO entrainment, the mPFC SO phase was determined from 0.5–2-Hz band-filtered LFPs. The instantaneous phase was computed as the Hilbert transform angle, and the phase distribution of each session was tested for uniformity. The SO phase modulation of SPW-Rs was determined using Rayleigh circular statistics (Berens, 2009; Ferraris et al., 2018).

2.4 | Tissue preparation and immunochemistry

After the abovementioned post-fixation, 50-µm coronal sections were obtained from the mPFC, CC, fimbria, and HPC (approximately bregma +1.70, +0.86, −0.82, and − 2.18 mm, respectively). Primary motor cortex (M1) and striatum correspond to the coordinates of CC. For node immunochemistry, slide-mounted slices were unmasked with sodium citrate for 15 min at 90°C. For all immunochemistries, slices were permeabilized in PBS with Triton 0.5% (T0.5%), followed by blocking in PBST0.5% with normal donkey serum 5% (NDS5%) for 60 min. Primary anti-MBP rat (1:100, Biorad), anti-SMI-32 mouse (1:200, Biolegend), anti-Olig2 rabbit (1:500, Merck), anti-CD140a rat (Pdgfra) (1:250, Merck), anti-CASPR mouse (1:200, DSHB), anti-GFP chicken (1:500, Aves Labs), and anti-Nav1.6 rabbit (1:500, Alomone Labs), antibodies diluted in PBST0.5% + NDS5% were used for 3 days at 4°C with agitation. Slices were washed with PBST0.1% four times for 10 min. Donkey anti-rat Alexa 488, anti-mouse Alexa 568, anti-rabbit Alexa 568, anti-rat Dye 647, anti-mouse Dye 647, and anti-chicken Alexa 488 (all 1:500, Jackson ImmunoResearch) were used as secondary antibodies. Nuclei were counterstained with Hoechst 33342 (1:1000, Sigma) diluted in PBST0.3%.

2.5 | Microscopy and image quantification

For Myelin Basic Protein (MBP) and SMI-32 fluorescence quantification, images were collected using a Zeiss Axio Imager 2 Apotome with 20× objective. Exposure duration was fixed for each brain structure

in order to be able to compare fluorescence intensity between animals. Mean fluorescence intensity was calculated using ImageJ software (NIH). MBP fluorescence was normalized taking as reference (100%) control values at each time point. All cuprizone-treated animals were compared to age matched controls to avoid differences due to late-occurring adult myelination.

For Olig2+ and Pdgfra+ cell counting, images were collected using a Zeiss Axio Imager 2 Apotome with 20× objective. Pdgfra+ cells were counted manually with Zen software and Olig2+ cells were counted semi-automatically with ImageJ software.

Internode images were collected using a Zeiss Axio Imager 2 Apotome with Zen software. High-magnification images (40× oil objective, 1-µm z-spacing) were collected using standard filters for DAPI (Hoechst), EGFP (Alexa 488), and CY5 (dye 647). To quantify internode length, GFP^+ internodes flanked by $CASPR^+$ paranodes were measured using ImageJ software with the "Simple Neurite Trace" script.

Node images were captured using a Zeiss LSM 780 confocal microscope with Zen Software. High-magnification images (63× oil objective, single z-plane) at 633-nm (dye 647) and 561-nm (Alexa 568) excitation were collected. Node lengths were quantified using nodes flanked by CASPR paranodes staining. To quantify mPFC node numbers and sizes, z-stacks corresponding to nine images (1-µm z-spacing) were analyzed. CC and fimbria analyses used images of a single z-plane. We averaged the node numbers per image. To measure node length, we used maximum intensity projection images (ImageJ software). To determine the node number per volume (mPFC) or surface (fimbria/CC), the node numbers in these images were averaged.

2.6 | Electron microscopy and g-ratio calculation

The samples were treated as described previously (Möbius et al., 2016). Mice were perfused with 2% paraformaldehyde/2.5% glutaraldehyde in PBS. After brain dissection, 100-µm vibratome sections of the mPFC, CC, and fimbria were left overnight in fixative. Then, 1.5-mm circular biopsy punches were high-pressure-frozen (Leica, EMPact2) using 20% BSA as cryoprotectant. The samples were cryosubstituted as follows: −90°C in 0.1% tannic acid in acetone for 96 h, four washes in acetone at −90°C for 2 h, post-fixation in OsO4 2%, uranyl acetate 0,1% in acetone at −90°C for 7 h. The samples were warmed over 14 h to −20°C and maintained for 16 h. Over 2.5 h, the samples were warmed to 4°C, then washed with acetone four times at room temperature for 1 h. Epon-embedded blocks were polymerized for 48 h at 60°C. Ultrathin sections (80 nm, Leica UC7) were deposited onto formvar-coated grids and counterstained using lead citrate and uranyl acetate. Images were acquired using a Tecnai G2 microscope at 200 keV with an Olympus Veleta camera.

Myelinated axon numbers and g-ratios (ratio of the axon diameter without myelin to that with myelin) were analyzed using AxonDeepSeg (Zaimi et al., 2018). Axon objects with diameter smaller than 0.1 µm were discarded from analysis, they did correspond to detection errors, the rest of detected axons were visually validated. At least 100 fibers per animal were analyzed using 4–5 animals per group.

2.7 | Western blotting

After brain extraction, 400-µm slices (MicroM vibratome) of the CC, mPFC, or HPC were dissected in cold HBSS (Invitrogen). Tissues were immediately frozen on dry ice, crushed, and sonicated in lysis buffer (1 mL/100 mg tissue; 50 mM Tris–HCl pH 7.5, 150 mM NaCl, 1 mM EDTA, 1 mM PMSF, anti-proteases, 1% Triton). Supernatants were collected after centrifugation (1 h, 14,000 rpm, 4°C). Proteins (20–40 µg load, quantified using Pierce BCA protein assay kit) were resolved by SDS/PAGE on 4–12% gels (Invitrogen) and blotted onto PVDF membranes. Membranes were blocked in TBS-T (0.02 M Tris pH 8, 0.5 M NaCl, 0.1% Tween-20) containing 4% dehydrated skim milk (overnight, 4°C) and incubated for 3–4 h with rabbit anti-GFAP (1:500, Dako), mouse anti-tau (1:1000, Millipore), rabbit anti-phospho-tau (pTau; 1:1000, Sigma), rabbit anti-synaptophysin 1 (1:2000, Sysy), mouse anti-amyloid precursor protein (APP; 1:200, Millipore), and rabbit anti-GAPDH (1:4000, Abcam) antibodies. Then, membranes were incubated with anti-rabbit or anti-mouse horseradish peroxidase-conjugated antibodies (1:3000; 1–2 h; Jackson ImmunoResearch) and visualized using ECL substrate (Lumi-Light Western Blotting Substrate; Pierce Chemical Company). Chemiluminescence was detected using the ECL Imager Chemi-Smart system (Fisher Bioblock).

2.8 | Behavioral tests general information

Prior to each behavioral experiment mice were gently handled once a day (minimum 3 min/mouse) in the behavioral room for at least 3 days before the start of the experiment. Mice were placed in the behavior room at least 45 min before testing. The apparatuses were cleaned with 30% ethanol between each mouse to remove odor cues, and the light was controlled. The order of animals was randomized for each test. For longitudinal studies, the order of the behavioral tasks was chosen to limit interferences between tests.

2.8.1 | Complex running wheel

Wheel cages (Lafayette Instrument Company, Inc.) that allowed for infrared-detected wheel rotation (Scurry Activity System) were used. Wheel speed was measured once at 1 min intervals. We calculated instantaneous and average speeds per 24 h period, as well as the accumulated distance run by each mouse. This complex wheel had 16 rungs removed to create a 22-rung repeat unit. The software was set up such that one revolution of the wheel (0.389 m traveled) represented 22 rungs. A 1 min interval was considered an activity when the distance traveled during the bin was >1 m/min. Single-caged mice ran spontaneously, without artificial rewards, for 1–9 km each night. Before the training, we clipped the whiskers of the mice to prevent them from detecting oncoming rungs in real-time. This protocol was adapted from a previous study (McKenzie et al., 2014).

2.8.2 | Open-field test

Mice were video-tracked in an open-field chamber (40 × 40 cm, white, high-density, non-porous plastic) using EthoVision software XT 16 (Noldus Inc.) following calibration according to the manufacturer's instructions. They were placed in the center to freely explore the chamber for 8 min. For analyses, the chamber was divided into center, border, and corner zones. We measured the total distance traveled, locomotion speed, and time and frequency of crossings in the three zones.

2.8.3 | Y-maze spontaneous alternation test

The Y-maze (Noldus) consisted of three white, high-density, nonporous plastic arms (each 35 cm long, 6 cm wide, 15 cm high; 120° between arms). Mice were video-tracked using EthoVision XT 16, and alternations were manually scored from these videos. Mice were placed in the starting arm facing the center and allowed to freely explore the maze for 8 min. A mouse has performed an arm entry when it places all four paws within the boundaries of the arm. An alternation was scored when all three arms were explored consecutively. The first two arm visits were considered samples. Subsequently, an alternation was recorded if the chosen arm has not been visited in the two previous choices. The percentage of alternations as an index of spatial working memory was calculated as follows: % alternation = [number of alternations/(total number of entries − 2)] × 100. If a mouse jumps out of the maze or does not move during the test, it is excluded from the analysis.

2.8.4 | Novel object recognition task

This task is based on the spontaneous preference of rodents for novelty and their memory ability (Ennaceur & Delacour, 1988). The open-field test arena was also used for the novel object recognition (NOR) test. Mice were habituated to the arena the day before task acquisition. Two identical objects were placed at opposite corners of the arena, 10 cm from the sidewalls. The test mouse was placed on the opposite side of the arena and allowed to explore for 10 min. After 1 h, one object was replaced with an object of similar size but different shape and color. Then, the same mouse was placed in the arena and allowed to explore the two (new and familiar) objects for 10 min. The movements were video-tracked using EthoVision XT 16. The exploration time of both objects (nose located in a 2 cm area around the object) was automatically measured using the software. The preference index (%) as an indicator of object recognition was calculated as follows: preference index = [exploration time of the new object/(exploration time of the new object + exploration time of the familiar object)] × 100. If a mouse does not reach a 20 s minimum of exploration for both objects at 10 min, we exclude it from the analysis, as it cannot be confirmed it spent enough time exploring to learn/discriminate.

2.8.5 | Three-chamber social preference test

The test was performed as described previously (Bertoni et al., 2021). The three-chamber apparatus consisted of a plexiglass box (50 × 25 cm) with a removable floor and partitions dividing the box into three chambers with 5 cm openings between chambers. The task consisted of four trials.

In the first trial (habituation), a test mouse was placed at the center of the apparatus, and two empty wire cages were placed in the left and right chambers to habituate the test mouse to the arena. The mouse was allowed to explore each chamber freely and was video-tracked for 5 min using EthoVision software. At the end of the trial, the animal was gently directed to the central chamber with the doors closed. In the second trial (social exploration), a same-aged C57BL/6J mouse (S1) was placed randomly in one of the two wire cages to avoid place preference. The second wire cage was empty (E). Then, the doors between the chambers were opened, and the test mouse was allowed to freely explore the arena for 10 min. At the end of the trial, the animal was gently directed to the central chamber with the doors closed. For the third trial (social discrimination), another C57BL/6J mouse of similar age (S2) was placed in the second wire cage. The test mouse had a choice between the familiar mouse (S1) and a stranger mouse (S2) for 10 min. At the end of the trial, each mouse was returned to its home cage for 30 min. In the fourth trial (short-term social memory), S2 was replaced with a new stranger mouse (S3), and the familiar mouse (S1) remained the same. The test mouse was allowed to explore the arena freely for 10 min. The time spent in each chamber and the time of contact with each wire cage (with a mouse or empty) were calculated using EthoVision software. The social interaction index was used to assess social exploration (sniffing time with S1/total time sniffing S1 + E × 100), social discrimination (sniffing time with S2/total sniffing time exploring S1 + S2 × 100), and short-term social memory (sniffing time S3/total time sniffing S1 + S3 × 100).

2.8.6 | Morris water maze test

We used a circular pool (120 cm diameter), in which mice were trained to escape from water (21 ± 1°C) by swimming to a hidden platform (1 cm beneath the surface), whose location could only be identified using distal extra-maze cues of different shapes and dimensions attached to the room walls. The pool was divided into four quadrants (intercardinal points: NE, NW, SW, and SE) using EthoVision XT 14. The platform was placed in the middle of the SW quadrant and remained there throughout the experiment. The spatial acquisition phase consisted of 16 training trials (4 training trials/day, 4 days, inter-trial interval ∼ 10 min). Mice were gently released with their heads facing the pool center and allowed to search for the platform for 60 s. The starting positions were semi-randomly changed. If the mice could not locate the platform after 60 s, they were manually guided to the platform and allowed to remain there for 30 s. The speed, latency, and path lengths required to reach the platform

were recorded. Before the first training day, the mice underwent acclimatization sessions (two trials of 60 s each) in a water maze with an emergent platform. The probe trials with the platform removed were performed 24 and 72 h after the acquisition phase. The mice were released from the center of the pool and allowed to swim freely for 60 s. The path was tracked and analyzed for the proportion of swim time or path length spent in each quadrant of the pool, and swim speed was recorded to assess spatial memory.

The following week, the same protocol was repeated with a novel platform position (middle of the NE quadrant) for 3 days of training (reversal training) and a 24-h reversal probe test to assess cognitive flexibility.

2.9 | Statistical analysis

Statistical analyses were performed using GraphPad Prism 8.0 (GraphPad Software, Inc., La Jolla, CA, USA). Because the data were according to the Kolmogorov–Smirnov test not normally distributed, the nonparametric Mann–Whitney U test was used for two-group comparisons. For multiple comparisons, a two-way ANOVA followed by Sidak's multiple comparison test was performed. Friedman's test was used in cases of repeated measures. To determine whether the median of a sample was equal to chance, we used the one-sample Wilcoxon signed-rank test. All statistical tests were two-tailed and tested against an alpha level $p < .05$.

For electrophysiological data, we performed estimation statistics, where median differences were calculated between CUP groups against a shared CTL group, and represented as Cumming estimation plots (lower panels in Figure 7b,c, Supplementary Figure S5). For each group, 5000 bootstrap samples were taken; the 95% confidence interval was bias-corrected and accelerated to account for the skew while obtaining the central 95% of the distribution (Ho et al., 2019). Reported permutation *p*-values are likelihoods of observing effect sizes if the null hypothesis of zero difference were true.

For histological and biochemical analyses, investigators were blinded to the experimental group. Because of cuprizone treatment and that the animals were not permanently marked, blinding was impossible for behavioral and electrophysiological experiments, but the investigators were blinded during data analyses.

3 | RESULTS

3.1 | Cuprizone-induced demyelination leads to short- and long-term cognitive impairment

Cuprizone intoxication is known to induce demyelination followed by spontaneous remyelination in the central nervous system of adult mice. First, we used the complex wheel test to monitor motor control and overall bilateral coordination associated with CC myelination (McKenzie et al., 2014). At W5, that is, at peak of demyelination, mice were trained for 1 week in a complex wheel. While CTL mice increased time spent in the running wheel during the first four nights before reaching a plateau, CUP mice decreased running time over the week (interaction treatment × nights: $p < .0001$). Thus, at night 7, CUP mice showed markedly reduced running time compared to CTL mice ($p = .0002$) (Supplementary Figure S1A). Furthermore, CUP mice also displayed a reduced progression of maximum running speed, an indicator of motor learning performance, along the training week as compared to CTL (interaction treatment × nights: $p < .0001$) (Supplementary Figure S1A). After 4 weeks of remyelination (W9), both maximum speed and running time normalized with no detectable differences between CTL and CUP W9 mice after 1 week of wheel training (CUP W9 vs CTL, night 7, maximum speed: $p = .767$; running time: $p > .999$) (Supplementary Figure S1A). These data indicate that remyelination leads to motor skill recovery.

We then performed longitudinal studies to evaluate the cognitive performance of mice at the demyelination peak (W5), 6 weeks after cuprizone removal (W11), and months after cuprizone removal (W22–W27). We first assessed spontaneous exploratory activity and anxiety-like behavior using the open-field test (Figure 1a,b). The total distance traveled is an index of exploratory behavior. During demyelination, this distance remained normal ($p = .8147$), but CUP mice exhibited exacerbated spontaneous activity after remyelination compared to CTL mice at W11 ($p = .0027$) and W22 ($p = .0295$), indicating hyperactivity (Figure 1b). CUP mice spent the same amount of time in the open-field center as CTL mice, indicating no signs of anxiety during demyelination or after remyelination (data not shown).

We investigated social behavior using a three-chamber test to assess sociability (social exploration), recognition of social novelty (social discrimination), and short-term social memory at W5, W11, and W22 (Figure 1c–f). The habituation phase showed no preference for any group, indicating no initial bias. In the sociability phase, both groups clearly preferred their congeneric over the empty cage at all time points. In the social novelty test, both groups strongly preferred the novel conspecific the familiar mouse at all time points, indicating preserved novelty discrimination (Figure 1d,e). However, in contrast to CTL mice, after a 30 min delay, CUP animals were no longer able to differentiate between the familiar and a novel mouse (social interaction index did not differ from chance, $p = .092$ at W5), indicating altered short-term social memory (Figure 1e). Interestingly, short-term social memory was still affected after remyelination (W11, $p = .339$; W22, $p = .147$) (Figure 1e). Measures of traveled distance in this test also indicated increased exploratory activity in CUP mice after remyelination at W11 (Figure 1f).

Memory modalities were further investigated using the NOR task and Y-maze test (W5, W11, W22–27), as well as the Morris water maze (W24–25). In the NOR task, no preference index differences between both groups were observed at any time point (W5, $p = .6730$; W11, $p = .0567$; W27, $p = .2991$) (Supplementary Figure S1B), indicating no deficit in recognition memory. A significantly increased total exploration time indicated hyperactivity in CUP mice at W11 (data not shown). In the Y-maze test, the percentage of correct alternations decreased during demyelination (W5, $p = .03$) and was not restored after remyelination (W11, $p = .0052$; W22,

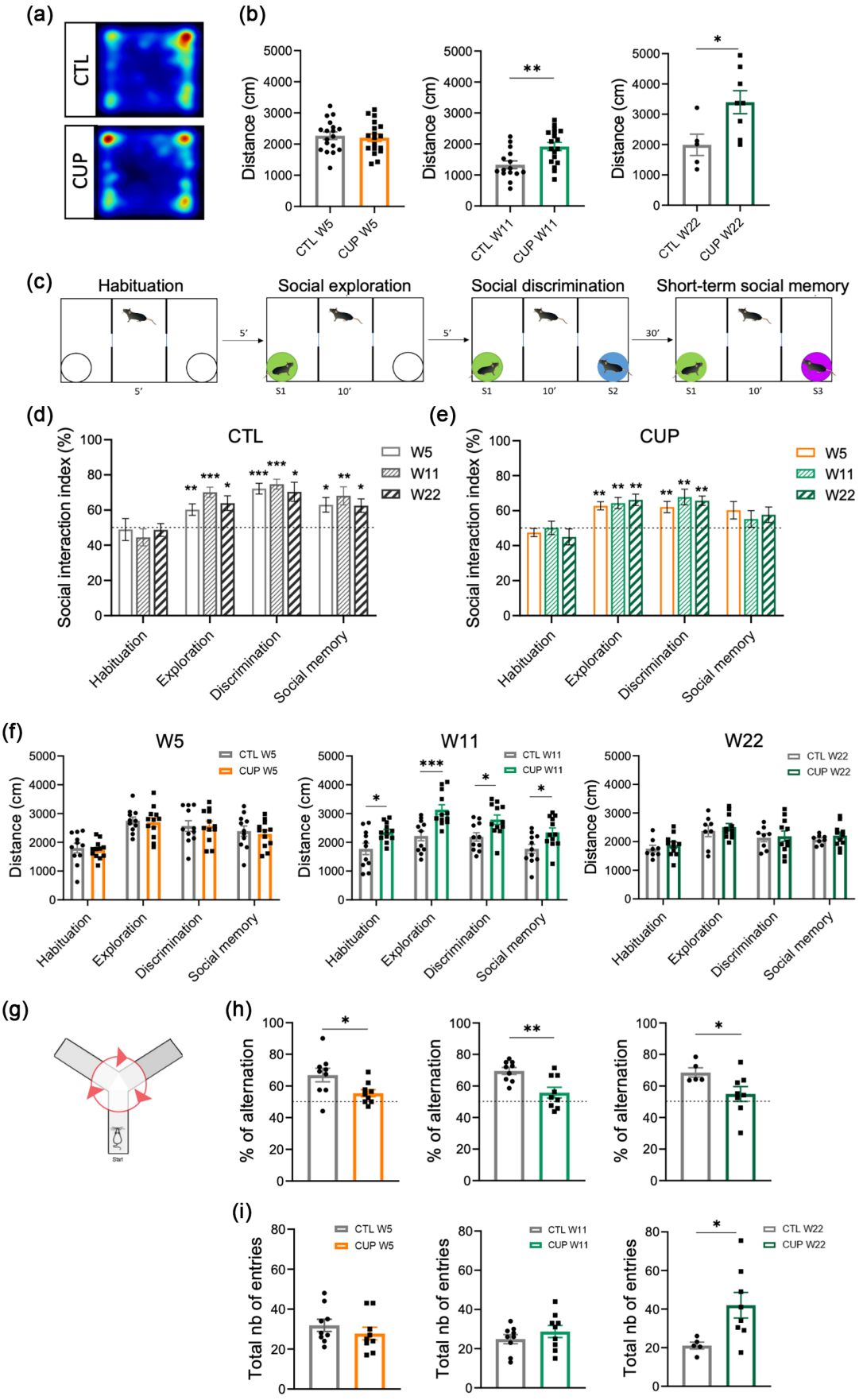

FIGURE 1 Legend on next page.

$p = .0295$) (Figure 1h), indicating persistently altered spatial working memory months after remyelination. Hyperactivity after remyelination was also observed in the Y-maze test at W22 ($p = .0186$) (Figure 1i).

Finally, we used the Morris water maze test to assess spatial learning, memory, and cognitive flexibility late after remyelination. During the first part (spatial training), remyelinated mice showed altered learning dynamics (time effect: $p = .1993$) compared to CTL (time effect: $p = .0443$) (Figure 2a), but memorized the platform location after 4 days of training like CTL mice, as demonstrated in the probe test 24 h (interaction treatment × quadrants: $p = .379$) (Figure 2b–d) and 72 h (not shown) after the training. However, during reversal learning, CUP mice failed to learn the new platform location (Figure 2e) (treatment effect: $p < .0001$; interaction treatment × days: $p = .033$; day 1: $p = .978$; day 2: $p = .0003$; day 3: $p = .0093$) and searched for the platform equally in all quadrants (Figure 2f–h) (interaction treatment × quadrants: $p = .0006$; time in target quadrant CTL vs. CUP: $p = .0239$), indicating preserved spatial memory but impaired cognitive flexibility.

Overall, our data indicate that a demyelination episode induces long-term impairment of specific cognitive functions, including spatial working memory, short-term social memory, and cognitive flexibility, as well as exploratory hyperactivity in animals. Thus, remyelination processes may be imperfect in brain areas associated with these modalities.

3.2 | Myelin content is reduced in the mPFC and HPC months after remyelination

Based on the above findings, we hypothesized that the number of oligodendrocyte lineage cells may be affected or that myelin content might not be restored in specific brain areas. We therefore analyzed MBP levels in different brain structures, with special focus on mPFC and HPC, which are involved in cognitive function, in addition to CC, which is typically analyzed in the cuprizone model.

MBP fluorescence was quantified at various time points following cuprizone treatment: at W5 (corresponding to the peak of demyelination after 5 weeks of cuprizone treatment), at 6 weeks after cuprizone removal (W11), and at 21 weeks after cuprizone removal (W26), as well as in age-matched control mice (Figure 3a and Supplementary Figure S2). As anticipated, the results reveal a significant drop in MBP levels at W5 in the CC, mPFC, M1,and HPC as compared to control values. The most substantial reductions were observed in the CC and M1, with decreases of 59% ± 8% and 71% ± 3%, respectively. The striatum was not affected, nor did the fimbria, as already described in the literature (Koutsoudaki et al., 2009). In all structures, MBP levels had returned to control values by W11. However, notably, in the PFC and HPC, a second phase of MBP decrease was observed at W26 (Figure 3b). In agreement with this observation, Western blot analysis after 5 months of remyelination (W26) showed that MBP expression in the CC was not different from control levels ($p = .0823$), whereas it was significantly decreased in the mPFC ($p = .0278$) and HPC ($p = .0025$) of CUP mice, indicating myelin deficit in these structures (Figure 3c, d).

We then examined whether reduced oligodendrocyte numbers may explain the reduction in myelin content after remyelination. At W26, $Olig2^+$ cell numbers did not differ between CUP and CTL mice in all analyzed structures (CC: $p = .1204$; mPFC: $p = .9974$; HPC: $p = .9969$) (Figure 3e). Among $Olig2^+$ cells, neither the numbers of OPCs identified by Pdgfra expression nor the numbers of $Olig2^+Pdgfra^-$ mature oligodendrocytes were affected (Figure 3).

These results indicate that a demyelination episode in mice leads to myelin recovery in the CC but not in gray matter structures as the mPFC and HPC, where myelin content is decreased despite recovering numbers of oligodendrocyte lineage cells.

To investigate possible axonal damage and neuronal degeneration, we assessed APP, pTau/Tau and SMI-32 as hallmarks of neuronal stress (Figure 4). SMI-32 immunofluorescence exhibited a significant increase in the mPFC at W5 ($p = .0159$), corresponding to the peak of demyelination (Figure 4a). However, SMI-32 levels returned to

FIGURE 1 A transient episode of demyelination induces long-term hyperactivity and impairment in social memory and spatial working memory. (a) Examples of heat maps of a CTL mouse and a CUP mouse after 5 weeks of cuprizone treatment. (b) Quantification of the total distance traveled by mice in the open field. Compared to CTL mice, the activity of CUP mice does not show significant changes after demyelination (W5), but it is increased after remyelination (W11 and W22). Dots represent single animal values in each group; bars represent mean ± SEM. W5: $n = 18$ CTL, $n = 18$ CUP; W11: $n = 15$ CTL, $n = 18$ CUP; W22: $n = 5$ CTL, $n = 8$ CUP. $^*p < .05$, $^{**}p < .01$. (c) Three-chambered mouse social paradigm. (d) Social interaction indexes show that CTL mice demonstrated clear social exploration, discrimination, and short-term memory at all time points analyzed. (e) Although CUP mice show unaffected social exploration and discrimination, their social interaction level index does not differ from chance-level performance at all time points for the last part of the test, indicating impaired short-term social memory. The dotted line depicts chance-level performance. Results are expressed as mean ± SEM. $n = 11$ CTL; $n = 12$ CUP. $^*p < .05$, $^{**}p < .01$, $^{***}p < .001$. (f) Average total distance traveled by CTL and CUP mice during each part of the three-chamber test at the three time points analyzed (W5, W11, W22). CUP mice exhibit hyperactivity at the first time point of remyelination (W11). Dots represent single animal values in each group; bars represent mean ± SEM. W5 and W11: $n = 11$ CTL, $n = 12$ CUP; W22: $n = 8$ CTL, $n = 11$ CUP. $^*p < .05$; $^{***}p < 10^{-3}$. (g) Schematic representation of Y-maze spontaneous alternation test for assessing spatial working memory. (h) CUP mice exhibit significantly fewer alternations (%) in the maze compared to CTL mice at all time points analyzed, indicating spatial working memory deficit after demyelination (W5) and remyelination (W11 and W22). (i) Average total number of entries of CTL and CUP mice at the three time points analyzed. While no differences were observed at W5 and W11, remyelinated mice exhibit hyperactivity at W22. Dotted line depicts chance level performance. Dots represent single animal values in each group; bars represent mean ± SEM. W5 and W11: $n = 9$ mice per group; W22: $n = 5$ CTL, $n = 8$ CUP. $^*p < .05$, $^{**}p < .01$.

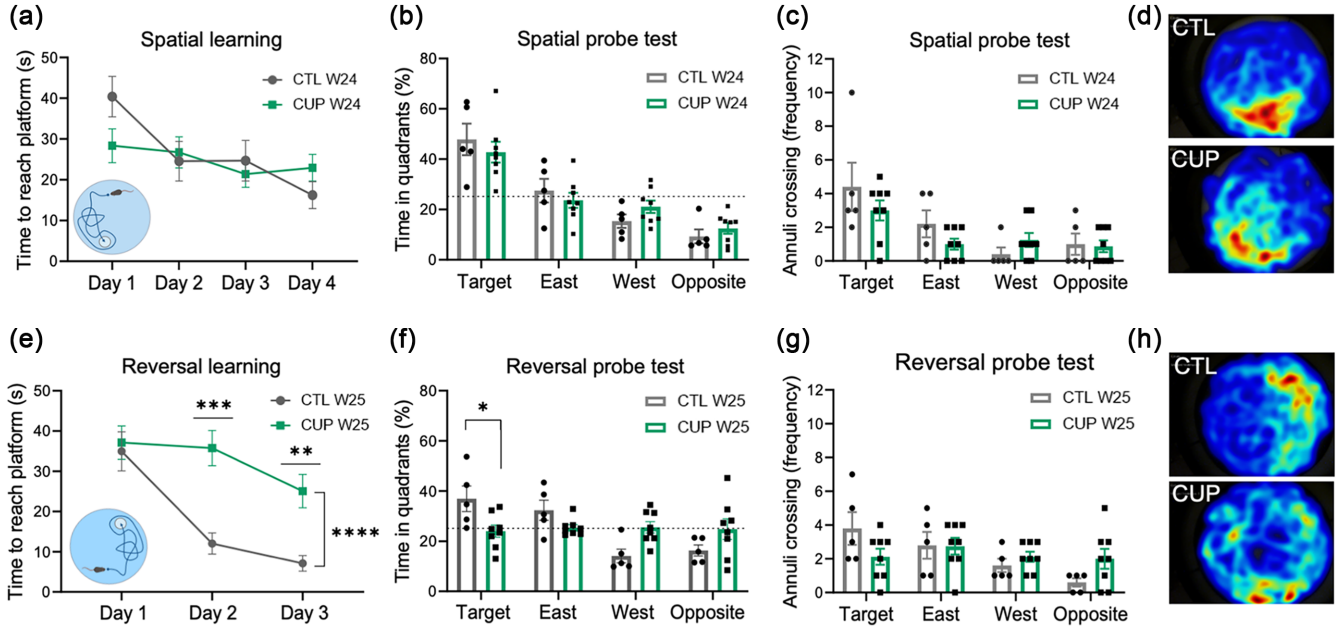

FIGURE 2 Cognitive flexibility is impaired 5 months after transient cuprizone-induced demyelination. (a) During the spatial learning phase, the mean time to reach the platform during the 4-day acquisition phase is not significantly different between CTL and CUP mice long after remyelination at W24. This time is reduced as the training progresses for CTL mice, but CUP mice show slightly altered learning dynamics with little progress between the first and last day of the training period. (b) During the spatial probe test, CTL and CUP mice spend more time searching for the platform in the target quadrant of the pool than in all others, indicating good spatial memory. (c) Average frequency of annuli crossing of CTL and CUP mice during spatial probe test. The annuli crossing represents the number of crosses over the platform site in the target quadrant and the crosses over corresponding sites in other quadrants. No difference is observed between CTL and CUP mice. (d) Representative heat maps of CTL and CUP mice during spatial probe test. (e) During reversal learning at W25, CUP mice show altered learning compared to CTL mice. (f) During the reversal probe test, remyelinated mice searched for the platform equally in all quadrants of the pool, indicating a deficit of cognitive flexibility. The dotted line depicts chance-level performance. (g) Average frequency of annuli crossing of CTL and CUP mice during reversal probe test. No difference is observed between the two groups but note that remyelinated mice seem to equally cross de four annuli, without preferentially crossing the target. Dotted line depicts chance level performance. Dots represent single animal values in each group; bars represent mean ± SEM. $n = 5$ CTL; $n = 8$ CUP. $^{*}p < .05$, $^{**}p < .01$, $^{***}p < .001$, $^{****}p < 10^{-4}$. (h) Representative heat maps of CTL and CUP mice during reversal probe test.

control values at W11 and W26. The other examined structures (CC and HPC) did not show any changes in SMI-32 after demyelination (not shown). No differences in APP and pTau/Tau expression were observed between cuprizone-treated and control mice in either structure (APP: mPFC $p = .3528$, HPC $p = .3232$; pTau /tau: mPFC $p = .3463$, HPC $p = .4040$) (Figure 4b,c). Beside, GFAP expression, a marker of gliosis, did not differ between the two groups in the mPFC at W26 ($p = .5581$) and HPC ($p = .7551$) (Figure 4b,c). In summary, these results collectively indicate no widespread neuronal degeneration 5 months after cuprizone treatment.

3.3 | Myelin structure is altered following a demyelination/remyelination episode

Once mature, internodes and nodes of Ranvier remain relatively stable, but remyelination changes the myelin architecture. In the adult brain, myelin produced during adaptive myelination is thinner with shorter internodes (Young et al., 2013), and the cortical myelin pattern is profoundly altered after remyelination (Orthmann-Murphy et al., 2020).

We performed immunostainings to determine whether the demyelination/remyelination episode in CUP mice induced long-term changes in the number and size of nodes of Ranvier. At W26, the number of Nav^{+} nodes flanked by CASPR paranodes was identical in the CC under both conditions ($p > .999$), but the nodes were shorter in CUP than in CTL mice ($p < 10^{-4}$) (Figure 5b). Conversely, the mPFC of CUP mice exhibited fewer ($p = .0345$) but longer ($p = .0155$) nodes (Figure 5d). The fimbria, containing HPC-mPFC projection fibers, tended to have fewer nodes without reaching significance ($p = .0565$) (Figure 5f), together with a decreased node length ($p < 10^{-4}$) (Figure 5f), as observed in the CC. We also examined the characteristics of nodes of Ranvier after short-term remyelination (W11) (Supplementary Figure S3). Consistent with our observations at W26, the nodes of CUP mice were shorter than those of CTL mice in the CC ($p < 10^{-4}$) and fimbria ($p < 10^{-4}$), but longer in the mPFC ($p = .0328$). No significant differences in node numbers were observed in any structure at W11 (CC: $p = .3044$; mPFC: $p = .8580$; fimbria: $p = .1903$) (Supplementary Figure S3A–C).

To examine the morphology of oligodendrocytes, we labeled a subset of mature oligodendrocytes by administering tamoxifen to

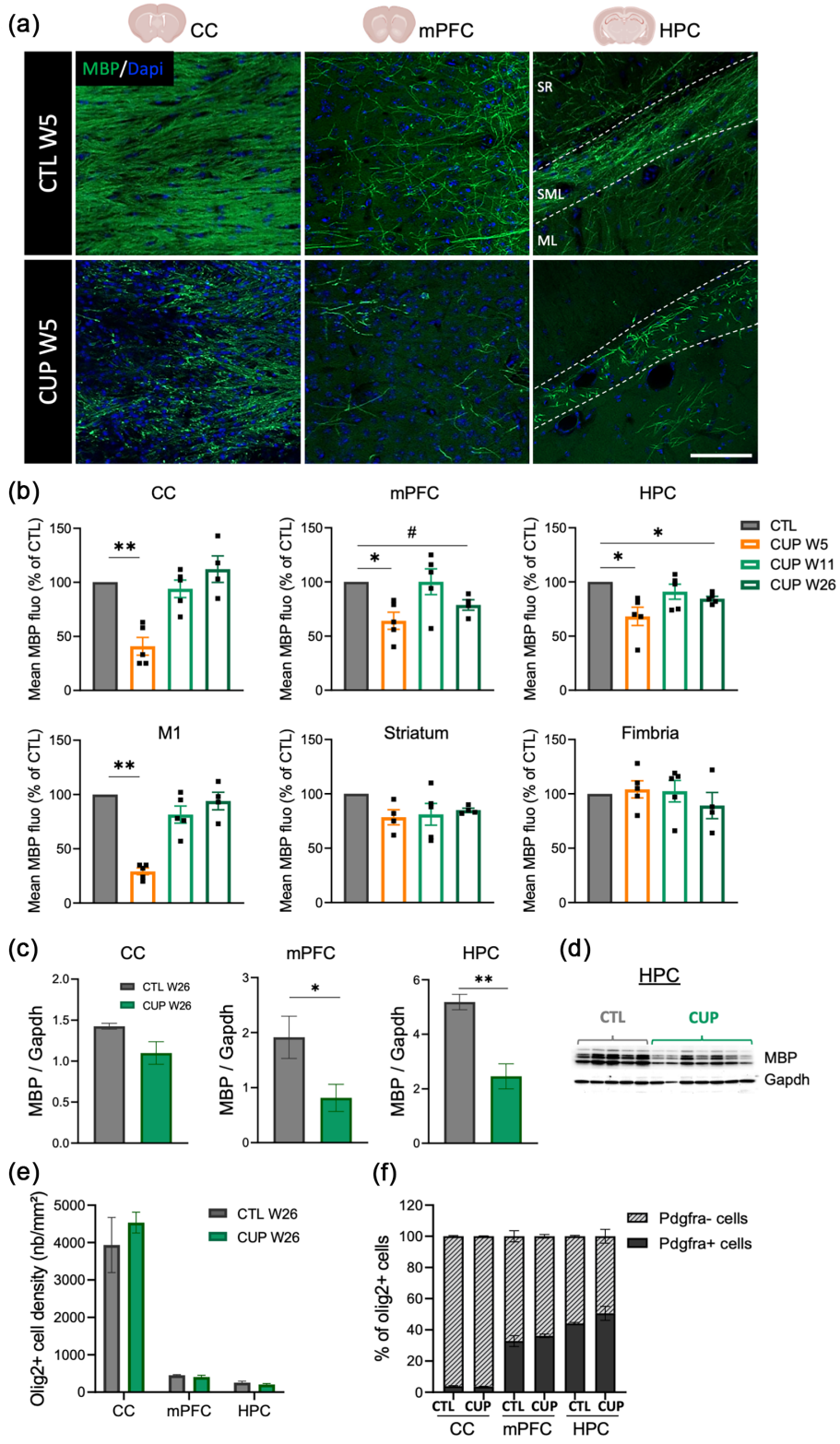

FIGURE 3 Myelin content is reduced in the mPFC and HPC several months after remyelination.(a) Apotome images of myelin (MBP, green) in medial CC, mPFC, and CA1 HPC (SR, stratum radiatum; SLM, stratum lacunosum-moleculare; ML, molecular layer) of CTL and CUP W5 mice. Scale bar = 50 µm. (b) Quantitative analysis of mean MBP fluorescence in medial CC, mPFC, CA1 HPC, M1, Striatum and Fimbria. For each CUP group, results are expressed as a percentage of respective CTL group mean (CTL W5, CTL W11, CTL W26). The CTL groups (100% value) have been pooled for graphical representation. Dots represent single animal values in each CUP group; bars represent mean ± SEM. $n = 3$ to 5 CTL per group. $n = 4$ to 5 CUP W5; $n = 5$ CUP W11; $n = 4$ CUP W26. $^{\#}p < .06$; $^{*}p < .05$, $^{**}p < .01$. (c) MBP expression analysis by western blotting in the CC, mPFC, and HPC of CTL and CUP mice at W26. While MBP expression is not affected in the CC, it is significantly reduced in the mPFC and HPC of CUP mice. Results are expressed as mean ± SEM. $n = 5$ CTL; $n = 7$ CUP. $^{*}p < .05$, $^{**}p < .01$. (d) Representative western blot of MBP protein in the HPC. (e) Quantitative analysis of $Olig2^{+}$ cell density in the CC, mPFC, and CA1 HPC showed no difference between CTL and CUP-treated mice at W26. (f) Co-labeling of $Olig2^{+}$ cells with Pdgfra revealed that the fraction of OPCs in all structures is not different between CTL and CUP mice at this late time point after demyelination. Results are expressed as mean ± SEM. $n = 3$ mice per group.

Plp-CreER:mTmG transgenic mice 24 h before sacrifice. The length of $mGFP^{+}$ internodes flanked by $CASPR^{+}$ paranodes in the mPFC (Figure 5g) was significantly increased at W26 ($p = .016$) (Figure 5h).

We then performed ultrastructural analyses to estimate myelin thickness at W26. Among the examined structures, the g-ratio was higher in CUP mice, indicating thinner regenerated myelin (CC: $p < 10^{-4}$; mPFC: $p = 0.0186$; fimbria: $p = .0002$) (Figure 6b,e,h). Interestingly, the myelinated axon density was decreased in the CC ($p = .0168$) and fimbria ($p < 10^{-4}$) but increased in the mPFC ($p = .0055$) compared to CTL animals (Figure 6c,f,i).

Taken together, these data indicate long-term structural modifications of newly formed myelin sheaths in the cuprizone model

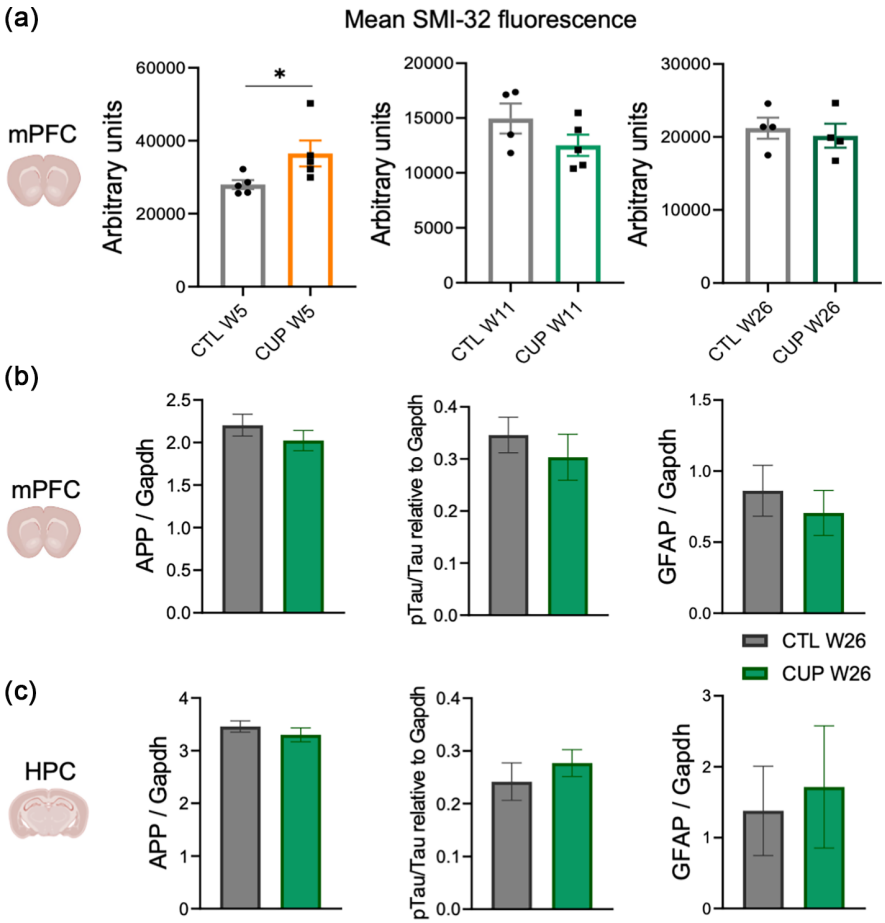

FIGURE 4 No signs of neuronal suffering 5 months after cuprizone treatment. (a) Quantitative analysis of mean SMI-32 fluorescence in the mPFC at W5, W11, and W26. While SMI-32 fluorescence was increased at W5 in CUP-treated mice compared to CTL, no difference was observed at W11 and W26. Dots represent single animal values in each CUP group; bars represent mean ± SEM. $n = 4$ to 5 CTL per group. $n = 5$ CUP W5; $n = 5$ CUP W11; $n = 4$ CUP W26. $^*p < .05$. Western blot analysis indicates no difference in APP, pTau/Tau and GFAP expression in the mPFC (b) and the HPC (c) between CTL and CUP mice at W26. Results are expressed as mean ± SEM. $n = 5$ CTL; $n = 7$ CUP.

of de- and remyelination. Defective myelination might prevent the restoration of normal activity in the HPC-mPFC network, thereby contributing to altered cognitive functions.

3.4 | HPC-mPFC network activity is altered during demyelination and only partially restored 4 months afterward

LFPs were recorded to assess HPC-mPFC network dynamics in CTL and CUP mice during demyelination and after remyelination. We used anesthesia as an "offline state" model, which displays the main hallmarks of HPC-mPFC coupling, as assessed by the synchrony between different LFP oscillations (Figure 7a) (Clawson et al., 2019; Ferraris et al., 2018).

During demyelination, we observed a decorrelation between HPC and mPFC LFPs, affecting two oscillatory couplings: within the high gamma band (60–120 Hz) and between HPC ripples and cortical SOs, compared to CTL mice (CUP W5 vs. CTL) (Figure 7b). SO and high gamma oscillation powers did not change in either the mPFC or HPC (Supplementary Figure S5, Supplementary Table 1); only their synchronization was affected (ripples/SO median correlation: CTL 0.47, CUP W5 0.09, $p < 10^{-4}$; high gamma median correlation: CTL 0.28, CUP W5 0.15, $p < 10^{-4}$). However, the HPC ripple power (Figure 7cA) was decreased (median: CTL 51.96 dB, CUP W5 43.62 dB, $p = .030$) without changing occurrence rate, duration, and mean frequency (Figure 7c-B,C,D; Table 1). Importantly, ripple/SO coupling was strongly impaired at W5, as measured by a drastic decrease in the strength of ripple entrainment by SO phase (CUP W5: mean phase 222.8 ± 68.3°, $R = 0.14 \pm 0.06$; CTL: mean phase 231.4 ± 6.9°, $R = 0.54 \pm 0.16$; mean phase comparison $p = .875$; R comparison $p = .004$) (Figure 7d).

At W11 and W20, the correlation between HPC and mPFC in the high gamma band was still decreased, although less pronounced (median correlation CUP W11 0.18 and W20 0.19, $p < 10^{-4}$ and $p = .034$, respectively) (Figure 7bB), and the lower gamma band (30–60 Hz) displayed a stronger correlation at W20 (median correlation CTL 0.19, CUP W20 0.33, $p < 10^{-4}$) (Figure 7bC), which was not present before (median correlation CUP W5 0.18 and CUP W11 1.19, $P = .0776$ and $p = .917$, respectively). Again, the mean power of SO and gamma bands was not significantly different from that of CTL mice (Supplementary Figure S5, Supplementary Table 1), and the ripple power appeared to be restored (median: CUP W11 49.51 dB, CUP W20 51.58 dB, $p = .234$ and $p = .767$, respectively) (Figure 7cA, Table 1). The ripple/SO coupling remained weakened (W11: 231.2 ± 12.5°, $R = 0.15 \pm 0.08$, mean phase comparison $p = .969$, R comparison $p = .0058$; W20: 229.1 ± 109.3°, $R = 0.11 \pm 0.06$, mean phase comparison $p = .63$, R comparison $p = .0358$) (Figure 7d).

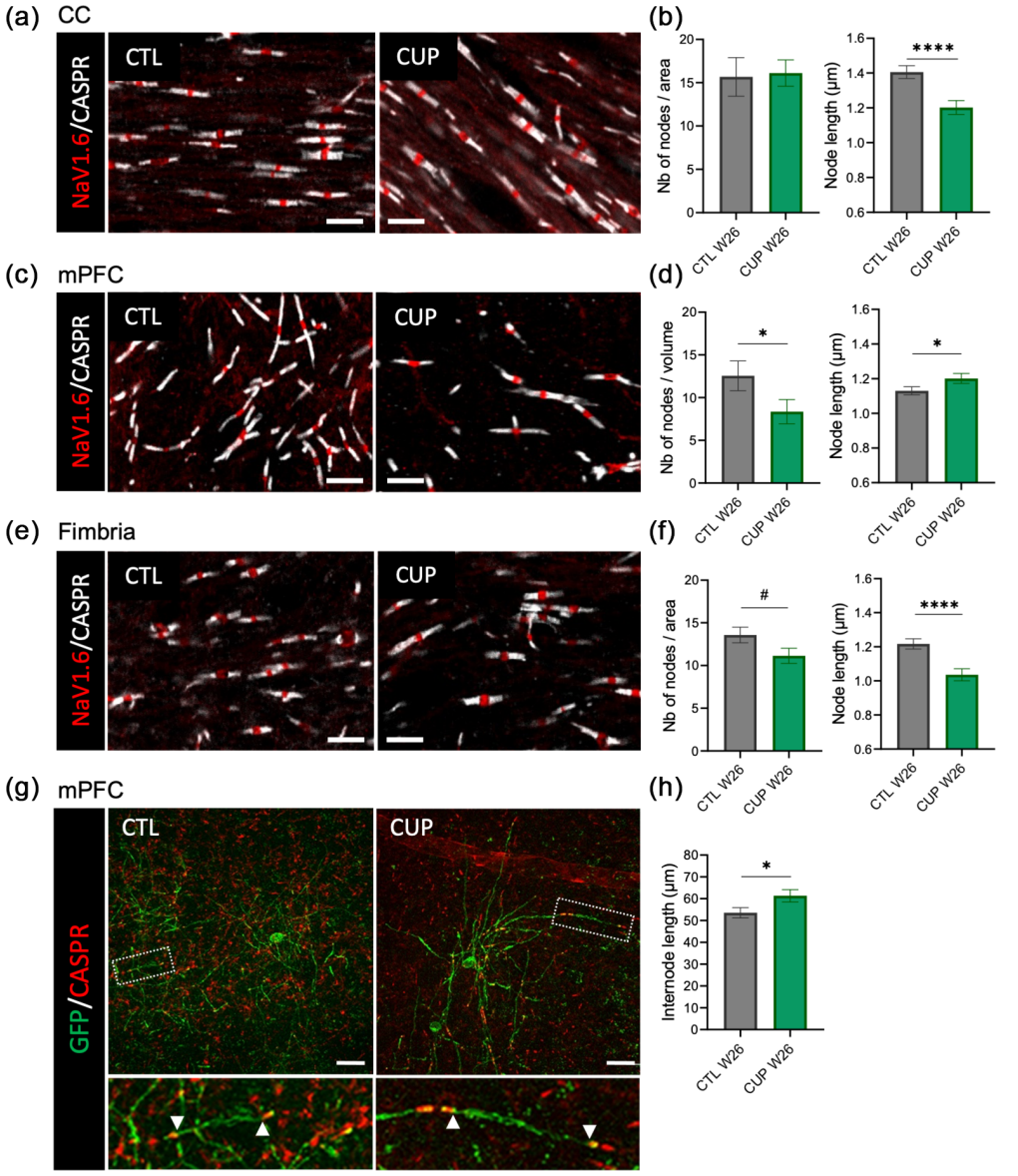

FIGURE 5 Five months after transient demyelination, regenerated myelin exhibits structural modifications. (a,c,e) Confocal images of nodes of Ranvier (Nav1.6, red) and paranodes (CASPR, white) and quantitative analysis of the number and length of nodes in the medial CC (b), mPFC (d), and fimbria (f) at W26. CC: $n = 141$ CTL nodes, $n = 145$ CUP nodes; mPFC: $n = 452$ CTL nodes, $n = 301$ CUP nodes; fimbria: $n = 195$ CTL nodes, $n = 159$ CUP nodes; 3 mice per group. $^{\#}p < .06$, $^{*}p < .05$, $^{****}p < .0001$. Scale bars = 5 µm. (g) Compressed confocal z-stacks of an mGFP^{+} (green) oligodendrocyte in the mPFC of *Plp-CreER:mTmG* transgenic CTL and CUP mice at W26. Arrowheads indicate the end of an internode, delimited by paranodes (CASPR, red). Scale bars = 20 µm. (h) Quantitative analysis of internode length in the mPFC of CTL and CUP mice at W26. Data are presented as median ± interquartile range. $n = 156$ CTL internodes, $n = 120$ CUP internodes; 3 mice per group. $^{*}p < .05$.

4 | DISCUSSION

Studies on demyelination/remyelination processes in cuprizone models have focused on a limited number of behavioral outcomes, and their histological and biochemical correlates have mostly been investigated in the CC. As the gray matter is also affected and its alteration may underlie various functional deficits, it seems critical to extend behavioral analyses to other modalities and identify their substrates in relevant CNS areas (Sen et al., 2019). The present study showed that after a demyelination episode in mice, remyelination did not restore all cognitive functions and was not identical among CNS areas. Although efficient in the CC, repair mechanisms were defective in the mPFC and HPC, as shown by long-term changes in myelin content and structure, which may affect neural information processing. Accordingly, these myelin modifications were associated with altered HPC-mPFC coupling, which may account for the observed cognitive deficits.

4.1 | Long-term impairment of cognitive behavior after a demyelination/remyelination episode in mice

Although cuprizone intoxication has been extensively used to investigate behavior during demyelination and after short-term remyelination, few studies have assessed its long-term effects, particularly on cognitive behavior (Sen et al., 2019). Here, we found that some cognitive functions were not affected after demyelination and remyelination, whereas others were impaired by demyelination and did not recover even after a long time following remyelination in CUP mice. This contrasts with the full restoration of motor skills in the complex wheel test. Likewise, recognition memory, as assessed by NOR, was preserved during demyelination/remyelination processes (Shimizu et al., 2023). The HPC may participate in object recognition memory, but this concept is debated (Inostroza et al., 2013; Lissner et al., 2021).

Previous studies using the Morris water maze have reported alterations in spatial learning and memory during demyelination

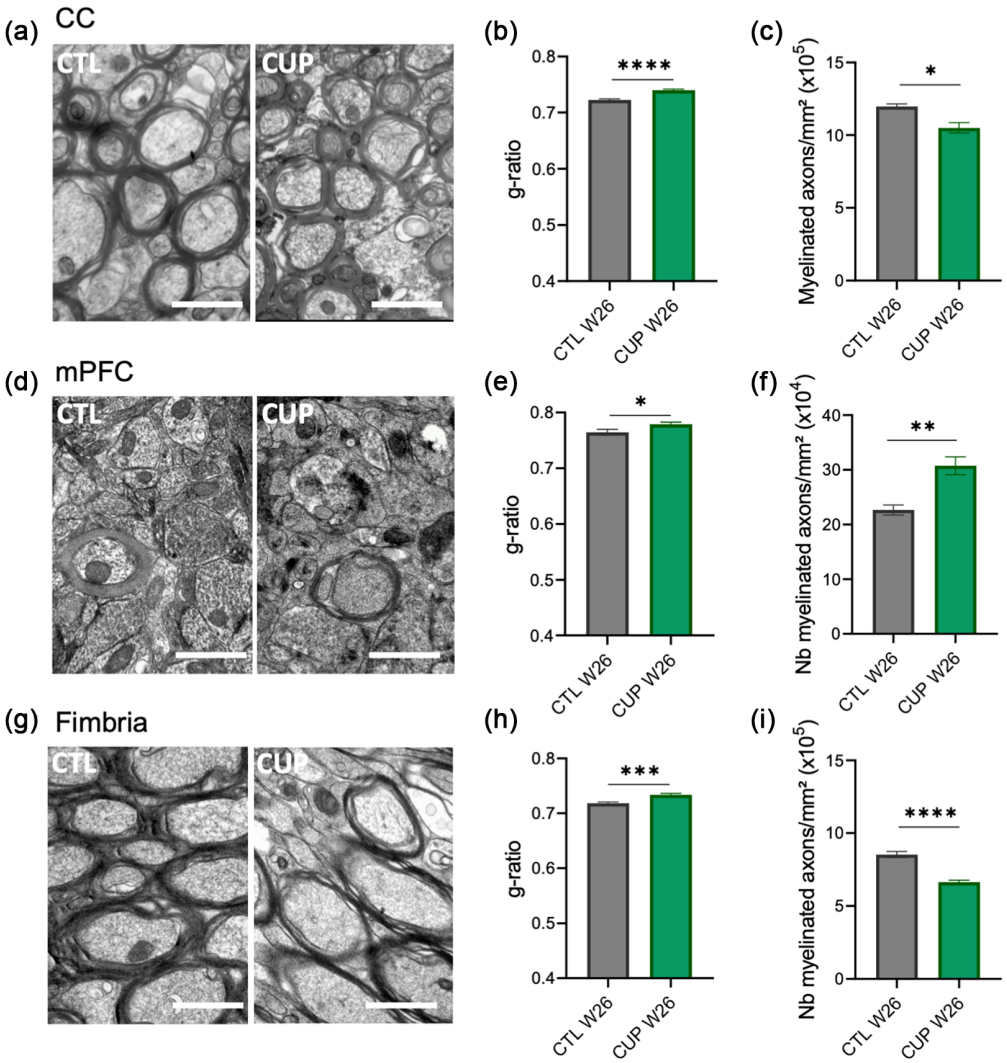

FIGURE 6 Five months after transient demyelination, the density of myelinated axons is altered, and regenerated myelin exhibits ultrastructural modifications. Transmission electron microscopy images of axons within the medial CC (a), mPFC (d), and fimbria (g) of CTL and CUP mice at W26. Quantitative analysis of the g-ratio in the CC (b), mPFC (e), and fimbria (h) at W26. Data are presented as median ± interquartile range. CC: $n = 3976$ CTL axons, $n = 3522$ CUP axons; mPFC: $n = 870$ CTL axons, $n = 1412$ CUP axons; fimbria: $n = 3318$ CTL axons, $n = 2481$ CUP axons; 4–5 mice per group. $^{*}p < .05$, $^{***}p < 0.001$, $^{****}p < 10^{-4}$. The density of myelinated axons in the CC (c), mPFC (f), and fimbria (i). Data are presented as median ± interquartile range. CC: $n = 100$ images per group; mPFC: $n = 116$ CTL images, $n = 138$ CUP images; fimbria: $n = 116$ CTL images, $n = 110$ CUP images; 4–5 mice per group. $^{*}p < .05$, $^{**}p < .01$, $^{****}p < 10^{-4}$. Scale bars = 1 μm.

(Aryanpour et al., 2017; Cui et al., 2018; Mohamed et al., 2019; Omotoso et al., 2018). Pharmacologically enhanced remyelination, especially in the HPC, strongly improves animal performances (Cui et al., 2018). At W24, we observed that spatial learning and memory were mostly normal. In contrast, CUP animals showed impaired spatial working memory (Y-maze) and short-term social memory (three-chamber test) during demyelination, and these behavioral deficits remained long after remyelination. These complex behaviors are known to depend on mPFC and HPC structures and their interactions (Churchwell & Kesner, 2011; Deng et al., 2019; Murray et al., 2015; Phillips et al., 2019; Spellman et al., 2015; Yoon et al., 2008). A very recent paper showed that oligodendrocyte production in the mPFC and HPC is required for working memory, but not for spatial or object recognition memory (Shimizu et al., 2023).

At W25, cognitive flexibility was impaired in the Morris water maze paradigm reflecting mPFC impairment (Guise & Shapiro, 2017; Murray et al., 2015; Ragozzino et al., 1999; Ragozzino et al., 2003). Interestingly, mPFC inactivation does not affect spatial learning and memory but impairs the ability to follow changing spatial rules (Guise & Shapiro, 2017). This is consistent with the original theory of Miller and Cohen and other studies, suggesting that during memory consolidation, the HPC allows memory formation, whereas the PFC manages flexibility between different memory traces depending on the context, avoiding interference (Eichenbaum, 2017; Miller & Cohen, 2001). Close interactions between these brain structures facilitate these complementary functions.

Finally, we demonstrated that after remyelination, CUP mice showed hyperactivity in the open-field test, as well as in the three-chamber test at W11 and Y-maze test at W22. Interestingly, locomotor hyperactivity is a typical behavioral abnormality of Alzheimer's disease mice, possibly linked to disinhibition (Gil-Bea et al., 2007). It may also reflect impaired attention processing and reaction to novelty, which may contribute to memory impairments (Verret et al., 2013). Furthermore, this behavior may reflect anxiety, similar to the defensive flight observed in mice exposed to environments that make them vulnerable (De Franceschi et al., 2016).

The observed cognitive alterations during demyelination are in agreement with a report that oligodendrocyte and myelin ablation in cortical gray matter is associated with cognitive disability in MS and that cortical lesion loads correlate with signs of physical and cognitive

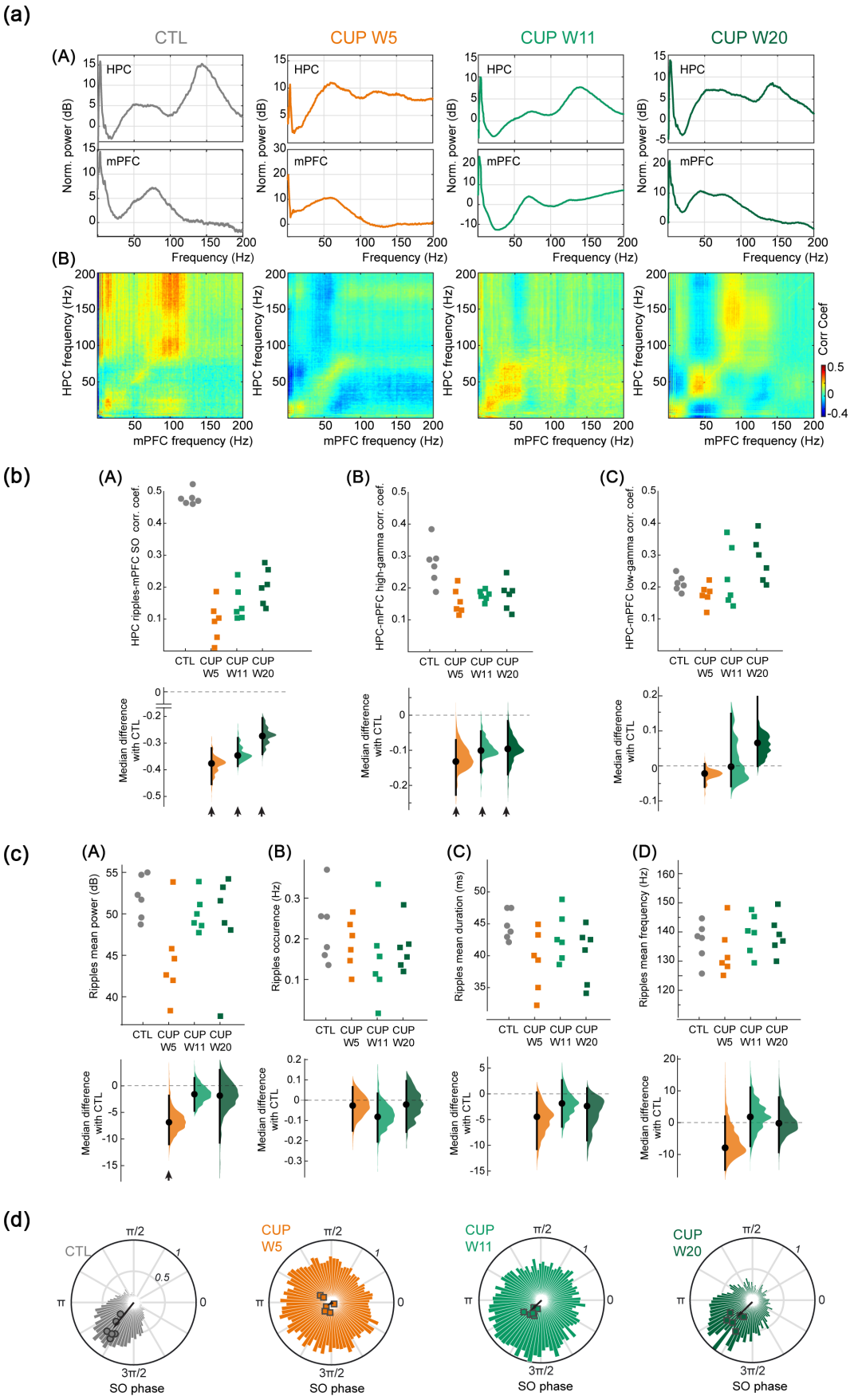

FIGURE 7 Legend on next page.

disability, including fatigue and memory loss (Calabrese et al., 2013). Specific deficits in attention and executive functions (including working memory and flexibility) have already been reported in MS patients (Brochet & Ruet, 2019; Cerezo García et al., 2015). Remyelination is efficient in some MS patients (Patrikios et al., 2006) and a robust mechanism in rodents. Numerous mouse model studies have shown that myelin can be restored by regenerating oligodendrocytes from resident progenitors. OPC repopulation and differentiation are much faster in the CC than in the cortex, suggesting delayed and incomplete remyelination in some CNS areas (Baxi et al., 2017; Gudi et al., 2009; Nyamoya et al., 2019). Moreover, several reports have shown that myelin integrity or remodeling is a key process for cognitive performance (Benamer et al., 2020; Chen et al., 2021; Eugenin von Bernhardi & Dimou, 2022; Pan et al., 2020; Steadman et al., 2020). Therefore, we hypothesized that the efficacy of the repair process may differ among brain regions, which might explain different behavioral outcomes.

4.2 | Quantitative and qualitative alterations of myelin several months after remyelination

Our data showed that after cuprizone-induced demyelination, the regenerative process is seemingly efficient in white matter fibers, which might account for the recovery of motor activity and coordination to control levels in the complex wheel 4 weeks after cuprizone removal. For instance, the myelin content in the CC of CUP mice returned to control values after remyelination. The node length decreases in this structure have been associated with increased conduction speed given constant channel numbers (Arancibia-Cárcamo et al., 2017; Lubetzki et al., 2020), which may reflect an efficient restoration of signal conduction. Furthermore, the number of nodes of Ranvier returned to normal in this structure. Conversely, we provided evidence for inadequate remyelination, both quantitatively and qualitatively, in the mPFC and HPC, which may explain persisting cognitive deficits after transient cuprizone-induced demyelination.

A recent study using time-lapse in vivo two-photon imaging of the somatosensory cortex followed the evolution of an oligodendrocyte subset during demyelination and remyelination. Only about half of the oligodendrocytes were replaced after 9 weeks of recovery, the authors estimated that approximately three additional months were required to reach the cortical oligodendrocyte density before cuprizone administration (Orthmann-Murphy et al., 2020). Our analyses showed that 5 months after cuprizone discontinuation, the cell density of the oligodendrocyte lineage had indeed returned to normal in all structures examined. However, at this time point, we observed an overall decrease in myelin content in both the HPC and mPFC, indicating incomplete remyelination of these gray matter structures.

Since demyelination can lead to axonal damage and neurodegeneration, we investigated the extent of such processes in our model. Our results suggest transient axonal suffering, specifically in the mPFC as revealed by significant increase in SMI-32 expression at peak of demyelination (W5) in this structure. Yet SMI-32 expression was no more elevated after remyelination and other markers such as pTau and APP were not altered either. A previous study has detected chronic axonal damage by SMI-32 staining during remyelination only after chronic demyelination (12 weeks cuprizone exposure) (Lindner et al., 2009). We thus believe that when behavioral experiments were performed, axonal damage was absent or undetectable.

We also analyzed node lengths in these structures, as well as internode lengths in the mPFC (high fiber density made this assessment impossible in the CC and fimbria). After remyelination, the restoration of conduction has been associated with shorter internodes (Lubetzki et al., 2020). In the mPFC, the internode length was increased, suggesting an imperfect restoration of signal conduction. Likewise, the number of nodes of Ranvier is reduced in this structure, and these nodes were longer than those in CTL animals. Increased lengths of nodes of Ranvier have been observed in MS (Howell et al., 2006) and aging (Hinman et al., 2006). Overall node length increases may contribute to altered function of myelinated axons in a

FIGURE 7 mPFC/HPC network activity is altered during demyelination and is only partially restored after 4 months of remyelination. (a, A) Representative examples of power spectra of HPC and mPFC LFPs recorded during anesthesia in CTL and CUP mice at the end of the demyelination (W5) and after remyelination (W11 and W20). The HPC spectrum shows a decrease in the ripple band (120–180 Hz) at W5, which tends to recover at W11 and W20. The other bands are not altered in their power. (B) Comodugrams depicting the cross-correlation of the HPC and mPFC LFP power spectra displayed in (A). Note the decrease in correlation at W5 particularly in the high gamma band and its partial recovery at W11 and W20. (B) Top row: distribution of the peak correlation coefficient extracted from the comodugrams in (a,B) showing the level of synchronization in (A) the HPC ripple band (120–180 Hz) and mPFC slow oscillations (SO, 1–2 Hz), (B) the HPC and mPFC high gamma band (60–120 Hz) that drops at W5 and tend to recover during the remyelination period, and (C) the HPC and mPFC low gamma band (30–60 Hz) that increases at W20. Each data point corresponds to an individual animal. The bottom row displays the median differences for 3 comparisons against the shared CTL (Cumming estimation plots), plotted as bootstrap sampling distributions. Each difference is depicted as a dot, and each 95% confidence interval is indicated by the ends of the vertical error bars (see Table 1 for corresponding statistics). Arrows indicate significant differences. (c) Top row: distribution of the ripples (A) mean power, (B) occurrence, (C) duration, and (D) mean frequency, showing no obvious difference between different time points in the demyelination/remyelination phases as compared to CTL animals, except for a decrease in ripple power in demyelinated mice (W5), which recovers at W11 and W20. The bottom row displays the median differences for three comparisons against the shared CTL. (d) Circular distributions of the entrainment of ripple occurrence by slow oscillation (SO) phase. The individual mean values (mean phase a function of the entrainment strength) are depicted by overlaid symbols (circles and squares). Black arrows indicate the mean phase and entrainment strength values. In demyelinated mice (W5), this ripple/SO coupling is lost as compared to CTL and tends to recover gradually from W11 to W20.

TABLE 1 Statistic table relative to Figure 7.

	Ripples/SO correlation coefficient		
	Unpaired median difference between CTL and	**95% confidence interval**	***p* value**
CUP W5	−0.38	(−0.46, −0.32)	<.0000
CUP W11	−0.35	(−0.30, −0.28)	<.0000
CUP W20	−0.27	(−0.34, −0.21)	<.0000
	High gamma correlation coefficient		
	Unpaired median difference between CTL and	**95% confidence interval**	***p* value**
CUP W5	−0.13	(−0.23, −0.07)	<.0000
CUP W11	−0.10	(−0.16, −0.05)	<.0000
CUP W20	−0.09	(−0.16, −0.02)	.0118
	Low gamma correlation coefficient		
	Unpaired median difference between CTL and	**95% confidence interval**	***p* value**
CUP W5	−0.02	(−0.06, 0.01)	.0776
CUP W11	0.00	(−0.06, 0.15)	.9170
CUP W20	0.09	(0.02, 0.17)	.0580
	Ripples occurrence (Hz)		
	Unpaired median difference between CTL and	**95% confidence interval**	***p* value**
CUP W5	−0.03	(−0.51, 0.07)	.0654
CUP W11	−0.08	(−0.21, 0.03)	.0335
CUP W20	−0.02	(−0.16, 0.10)	.6240
	Ripples mean duration (s)		
	Unpaired median difference between CTL and	**95% confidence interval**	***p* value**
CUP W5	−4.45	(−10.80, 0.30)	.0216
CUP W11	−1.85	(−6.40, 2.70)	.3970
CUP W20	−2.30	(−8.59, 1.18)	.0892
	Ripples mean frequency (Hz)		
	Unpaired median difference between CTL and	**95% confidence interval**	***p* value**
CUP W5	−7.93	(−15.0, 2.02)	.1580
CUP W11	1.83	(−7.44, 11.20)	.6520
CUP W20	−0.17	(−8.60, 8.22)	.9200
	Ripples mean power (dB)		
	Unpaired median difference between CTL and	**95% confidence interval**	***p* value**
CUP W5	−8.35	(−13.0, −2.74)	.0300
CUP W11	−2.45	(−5.95, 0.96)	.2340
CUP W20	−1.85	(−10.3, 2.83)	.4880
	SO mean power (dB)		
	Unpaired median difference between CTL and	**95% confidence interval**	***p* value**
CUP W5	−3.86	(−17.80, 9.90)	.6240
CUP W11	−1.50	(−11.42, 8.41)	.7130
CUP W20	0.57	(−13.10, 11.20)	.9380
	SO mean frequency (Hz)		
	Unpaired median difference between CTL and	**95% confidence interval**	***p* value**
CUP W5	−0.03	(−0.72, 0.53)	.7950
CUP W11	0.09	(0.56, 0.76)	.7290

TABLE 1 (Continued)

	SO mean frequency (Hz)		
	Unpaired median difference between CTL and	**95% confidence interval**	***p* value**
CUP W20	−0.03	(−0.72, 0.53)	.8030
	HPC low gamma mean power (dB)		
	Unpaired median difference between CTL and	**95% confidence interval**	***p* value**
CUP W5	−1.49	(−9.65, 6.29)	0.7690
CUP W11	−1.25	(−10.80, 4.74)	0.6580
CUP W20	−2.85	(−12.90, 8.45)	0.6250
	mPFC low gamma mean power (dB)		
	Unpaired median difference between CTL and	**95% confidence interval**	***p* value**
CUP W5	4.41	(−2.19, 6.13)	0.0654
CUP W11	1.45	(−5.01, 6.13)	0.6010
CUP W20	1.39	(−5.20, 5.36)	0.4520
	HPC high gamma mean power (dB)		
	Unpaired median difference between CTL and	**95% confidence interval**	***p* value**
CUP W5	2.73	(−5.37, 8.38)	0.6130
CUP W11	0.96	(−6.21, 5.4)	0.8670
CUP W20	−1.81	(−9.42, 5.54)	0.6430
	mPFC high gamma mean power (dB)		
	Unpaired median difference between CTL and	**95% confidence interval**	***p* value**
CUP W5	3.56	(−3.48, 7.40)	.4780
CUP W11	4.72	(−2.32, 7.76)	.4810
CUP W20	1.41	(−4.36, 6.36)	.5460

wide range of diseases leading to conduction disruption (Arancibia-Carcamo & Attwell, 2014).

In the fimbria, which contain myelinated HPC-mPFC projections (Jay & Witter, 1991), node numbers did not significantly differ from those in the CTL group, although there was a decreasing trend in remyelinated animals. Similar to the CC, the node length was reduced, suggesting a better repair process in this structure; however, fimbria is seemingly less affected by cuprizone-induced demyelination than the HPC (Koutsoudaki et al., 2009), which might account for better recovery.

Finally, we found that more than 5 months after cuprizone treatment, regenerated myelin was thinner (higher g-ratio) in all structures examined. In rodents, myelin synthesized in adulthood or during repair is thinner than myelin produced during physiological development (Lasiene et al., 2009; Young et al., 2013). We found lower myelinated axon densities in the CC and fimbria of remyelinated animals, but higher densities in the mPFC. Because oligodendrocyte numbers were normal in all structures, this increase in the mPFC could be attributed to the higher internode length, which increased the probability of finding myelinated axons in transverse sections.

All observed changes (myelin thickness, internode and node length) have been suggested as axon-glial parameters that strongly influence the fine-tuning of axonal conduction speed to meet information processing needs at the network scale (Arancibia-Cárcamo et al., 2017; Cullen et al., 2021; Harris & Attwell, 2012; Lubetzki et al., 2020). Based on previous data (Lubetzki et al., 2020), the increase in node and internode lengths and decrease in myelin thickness observed in the mPFC could lead to a decrease in action potential conduction velocity, possibly disrupting network activity.

4.3 | A demyelination episode durably alters HPC-mPFC synchronization despite remyelination

HPC–mPFC fine-coupling is involved in memory processing and context-guided behavior (Eichenbaum, 2017; Peng & Burwell, 2021). Therefore, we tested the hypothesis that in our model, the altered myelin content and structure occurring in these areas might be associated with coupling defects. Using electrophysiological recordings in anesthetized mice, we tested whether basic coupling was affected, potentially a substrate for observed cognitive deficits. The demyelination episode caused lasting disruptions in two hallmarks of synchronization between HPC and mPFC activity: gamma synchronization and ripple/SO coupling.

Gamma oscillations can be observed during both sleep and wakefulness (Buzsáki & Wang, 2012), and their synchronization is assumed

to promote inter-regional communication (Buzsáki & Schomburg, 2015; Ferraris et al., 2018; Fries, 2015). They are associated with different memory processes, such as memory retrieval (Colgin et al., 2009), spatial memory/navigation (Montgomery & Buzsáki, 2007), and working memory (Yamamoto et al., 2014). Gamma oscillations rely on the activity of parvalbumin (PV)-containing GABAergic neurons (i.e., PV basket cells) (Csicsvari et al., 2003; Mann et al., 2005; Wang & Buzsáki, 1996), which form large interconnected networks both in the cortex and HPC, and interact with excitatory principal cells (Galarreta & Hestrin, 2002; Traub et al., 2018). Myelination of PV basket cells is required to preserve the physiological dynamics of local circuit synchronization (Dubey et al., 2022). Their deficient remyelination after demyelination may explain the persistent gamma synchronization deficit observed in W11 and W20 mice, possibly contributing to memory-related deficits in those mice.

Hippocampal ripples and SOs are coupled during sleep, which is instrumental in different learning and memory processes (Battaglia et al., 2004; Maingret et al., 2016; Todorova & Zugaro, 2018). Ripples also depend on the activity of GABAergic neurons, including PV basket cells (Buzsáki et al., 2012), and the observed alteration in ripple power may be caused by insufficient remyelination of these neurons. Moreover, the HPC is connected mostly unidirectionally to the mPFC through long-range connections, which are most likely myelinated (Nickel & Gu, 2018), and myelin is important to maintain synchronization through long-range axons involved in cognitive processes (Kato & Wake, 2021). Interestingly, the fact that myelin most likely controls the spike timing and fine-tuning of network synchronization (Bells et al., 2017; Noori et al., 2020) is in accordance with the observed deficits in HPC-mPFC oscillatory coupling and HPC ripple power, which depend on fine-tuned spike timing of the hippocampal network (Szabo et al., 2022). Therefore, the observed persistent inadequacy in SO/ripple phase coupling in demyelinated/remyelinated animals may also explain their long-term cognitive deficits.

In conclusion, this study shows that despite remyelination, CUP animals retain long-term impairment of cognitive functions that involve HPC-mPFC fine-coupling (Eichenbaum, 2017; Peng & Burwell, 2021), including social memory, spatial working memory, and cognitive flexibility. These mice also exhibit hyperactivity after remyelination not observed during demyelination. As potential substrates of these behavioral deficits, we provide evidence for altered oscillatory coupling between the HPC and mPFC, two structures showing persistent reductions in myelin content and changes in myelin structure. Altogether, the myelin self-repair process, although robust in rodents, is heterogeneous among brain regions, inducing different behavioral and functional outcomes ranging from beneficial to detrimental. Further understanding of mechanisms underlying failures in these processes is of major interest in the field of demyelinating diseases, particularly for the development of treatments aimed at optimizing remyelination processes and, thus, functional recovery.

AUTHOR CONTRIBUTIONS

OM designed and conducted the experiments and wrote the manuscript. PQ performed electrophysiological analyses and wrote the manuscript. KM, FG, FR, and AG conducted experiments and commented on the manuscript. MC designed the experiments, co-supervised the project, and commented on the manuscript. PD designed the experiments, supervised the project, and wrote the manuscript.

ACKNOWLEDGMENTS

We are grateful to Lydia Kerkerian-le Goff (IBDM) for discussions and critical reading of the manuscript. We thank Monique Esclapez for advice on neuroanatomy, Sébastien Lopez and Claire Rampon for their help and expertise in behavioral analyses, and the LNC behavioral platform for their help in setting up the tests. We thank Stéphane Gaillard (Phenotype Expertise) for his technical advice on behavioral analyses; Phenotype Expertise performed the three-chamber test. Nicolas Brouilly and Aicha Aouane assisted with the electron microscopy on the IBDM platform.

FUNDING INFORMATION

This work was funded by CNRS, Aix-Marseille University, and the ARSEP Foundation. We also acknowledge the France-Bioimaging/PICSL infrastructure (ANR-10-INSB-04-01), NeuroMarseille Institute, and NeuroSchool/nEURo*AMU (ANR-17-EURE-0029).

CONFLICT OF INTEREST STATEMENT

The authors declare no competing interests.

DATA AVAILABILITY STATEMENT

This study did not generate new unique reagents. Further information and requests for reagents may be directed to, and will be fulfilled by the corresponding author.

ORCID

Pascale Durbec https://orcid.org/0000-0002-9660-1809

REFERENCES

Arancibia-Carcamo, I. L., & Attwell, D. (2014). The node of Ranvier in CNS pathology. *Acta Neuropathologica*, *128*(2), 161–175. https://doi.org/10.1007/s00401-014-1305-z

Arancibia-Cárcamo, I. L., Ford, M. C., Cossell, L., Ishida, K., Tohyama, K., & Attwell, D. (2017). Node of Ranvier length as a potential regulator of myelinated axon conduction speed. *eLife*, *6*, e23329. https://doi.org/10.7554/eLife.23329

Aryanpour, R., Pasbakhsh, P., Zibara, K., Namjoo, Z., Beigi Boroujeni, F., Shahbeigi, S., Kashani, I. R., Beyer, C., & Zendehdel, A. (2017). Progesterone therapy induces an M1 to M2 switch in microglia phenotype and suppresses NLRP3 inflammasome in a cuprizone-induced demyelination mouse model. *International Immunopharmacology*, *51*, 131–139. https://doi.org/10.1016/j.intimp.2017.08.007

Bacmeister, C. M., Barr, H. J., McClain, C. R., Thornton, M. A., Nettles, D., Welle, C. G., & Hughes, E. G. (2020). Motor learning promotes remyelination via new and surviving oligodendrocytes. *Nature Neuroscience* Published online May 18, *7*, 1–13. https://doi.org/10.1038/s41593-020-0637-3

Battaglia, F. P., Sutherland, G. R., & McNaughton, B. L. (2004). Hippocampal sharp wave bursts coincide with neocortical "up-state" transitions. *Learning & Memory*, *11*(6), 697–704. https://doi.org/10.1101/lm.73504

Baxi, E. G., DeBruin, J., Jin, J., Strasburger, H. J., Smith, M. D., Orthmann-Murphy, J. L., Schott, J. T., Fairchild, A. N., Bergles, D. E., & Calabresi, P. A. (2017). Lineage tracing reveals dynamic changes in oligodendrocyte precursor cells following cuprizone-induced demyelination. *Glia*, *65*(12), 2087–2098. https://doi.org/10.1002/glia.23229

Bells, S., Lefebvre, J., Prescott, S. A., Dockstader, C., Bouffet, E., Skocic, J., Laughlin, S., & Mabbott, D. J. (2017). Changes in white matter microstructure impact cognition by disrupting the ability of neural assemblies to synchronize. *The Journal of Neuroscience*, *37*(34), 8227–8238. https://doi.org/10.1523/JNEUROSCI.0560-17.2017

Benamer, N., Vidal, M., Balia, M., & Angulo, M. C. (2020). Myelination of parvalbumin interneurons shapes the function of cortical sensory inhibitory circuits. *Nature Communications*, *11*(1), 5151. https://doi.org/10.1038/s41467-020-18984-7

Berens, P. (2009). CircStat : A MATLAB toolbox for circular statistics. *Journal of Statistical Software*, *31*(10), 1–21. https://doi.org/10.18637/jss.v031.i10

Bertoni, A., Schaller, F., Tyzio, R., Gaillard, S., Santini, F., Xolin, M., Diabira, D., Vaidyanathan, R., Matarazzo, V., Medina, I., Hammock, E., Zhang, J., Chini, B., Gaiarsa, J. L., & Muscatelli, F. (2021). Oxytocin administration in neonates shapes hippocampal circuitry and restores social behavior in a mouse model of autism. *Molecular Psychiatry*, *26*(12), 7582–7595. https://doi.org/10.1038/s41380-021-01227-6

Brochet, B., & Ruet, A. (2019). Cognitive impairment in multiple sclerosis with regards to disease duration and clinical phenotypes. *Frontiers in Neurology*, *10*, 261. https://doi.org/10.3389/fneur.2019.00261

Brousse, B., Magalon, K., Durbec, P., & Cayre, M. (2015). Region and dynamic specificities of adult neural stem cells and oligodendrocyte precursors in myelin regeneration in the mouse brain. *Biology Open*, *4*(8), 980–992. https://doi.org/10.1242/bio.012773

Buzsáki, G., Anastassiou, C. A., & Koch, C. (2012). The origin of extracellular fields and currents—EEG, ECoG, LFP and spikes. *Nature Reviews Neuroscience*, *13*(6), 407–420. https://doi.org/10.1038/nrn3241

Buzsáki, G., & Schomburg, E. W. (2015). What does gamma coherence tell us about inter-regional neural communication? *Nature Neuroscience*, *18*(4), 484–489. https://doi.org/10.1038/nn.3952

Buzsáki, G., & Wang, X. J. (2012). Mechanisms of gamma oscillations. *Annual Review of Neuroscience*, *35*, 203–225. https://doi.org/10.1146/annurev-neuro-062111-150444

Calabrese, M., Favaretto, A., Poretto, V., Romualdi, C., Rinaldi, F., Mattisi, I., Morra, A., Perini, P., & Gallo, P. (2013). Low degree of cortical pathology is associated with benign course of multiple sclerosis. *Multiple Sclerosis*, *19*(7), 904–911. https://doi.org/10.1177/1352458512463767

Cerezo García, M., Martín Plasencia, P., & Aladro, B. Y. (2015). Alteration profile of executive functions in multiple sclerosis. *Acta Neurologica Scandinavica*, *131*(5), 313–320. https://doi.org/10.1111/ane.12345

Chen, J. F., Liu, K., Hu, B., Li, R. R., Xin, W., Chen, H., Wang, F., Chen, L., Li, R. X., Ren, S. Y., Xiao, L., Chan, J. R., & Mei, F. (2021). Enhancing myelin renewal reverses cognitive dysfunction in a murine model of Alzheimer's disease. *Neuron*, *109*(14), 2292–2307.e5. https://doi.org/10.1016/j.neuron.2021.05.012

Chiaravalloti, N. D., & DeLuca, J. (2008). Cognitive impairment in multiple sclerosis. *Lancet Neurology*, *7*(12), 1139–1151. https://doi.org/10.1016/S1474-4422(08)70259-X

Chorghay, Z., Káradóttir, R. T., & Ruthazer, E. S. (2018). White matter plasticity keeps the brain in tune: Axons conduct while glia wrap. *Frontiers in Cellular Neuroscience*, *12*, 428. https://doi.org/10.3389/fncel.2018.00428

Churchwell, J. C., & Kesner, R. P. (2011). Hippocampal-prefrontal dynamics in spatial working memory: Interactions and independent parallel processing. *Behavioural Brain Research*, *225*(2), 389–395. https://doi.org/10.1016/j.bbr.2011.07.045

Clawson, W., Vicente, A. F., Ferraris, M., Bernard, C., Battaglia, D., & Quilichini, P. P. (2019). Computing hubs in the hippocampus and cortex. *Science Advances*, *5*(6), eaax4843. https://doi.org/10.1126/sciadv.aax4843

Colgin, L. L., Denninger, T., Fyhn, M., Hafting, T., Bonnevie, T., Jensen, O., Moser, M. B., & Moser, E. I. (2009). Frequency of gamma oscillations routes flow of information in the hippocampus. *Nature*, *462*(7271), 353–357. https://doi.org/10.1038/nature08573

Csicsvari, J., Jamieson, B., Wise, K. D., & Buzsáki, G. (2003). Mechanisms of gamma oscillations in the hippocampus of the behaving rat. *Neuron*, *37*(2), 311–322. https://doi.org/10.1016/s0896-6273(02)01169-8

Cui, C., Wang, J., Mullin, A. P., Caggiano, A. O., Parry, T. J., Colburn, R. W., & Pavlopoulos, E. (2018). The antibody rHIgM22 facilitates hippocampal remyelination and ameliorates memory deficits in the cuprizone mouse model of demyelination. *Brain Research*, *1694*, 73–86. https://doi.org/10.1016/j.brainres.2018.05.013

Cullen, C. L., Pepper, R. E., Clutterbuck, M. T., Pitman, K. A., Oorschot, V., Auderset, L., Tang, A. D., Ramm, G., Emery, B., Rodger, J., Jolivet, R. B., & Young, K. M. (2021). Periaxonal and nodal plasticities modulate action potential conduction in the adult mouse brain. *Cell Reports*, *34*(3), 108641. https://doi.org/10.1016/j.celrep.2020.108641

Dawson, M. (2003). NG2-expressing glial progenitor cells: An abundant and widespread population of cycling cells in the adult rat CNS. *Molecular and Cellular Neuroscience*, *24*(2), 476–488. https://doi.org/10.1016/S1044-7431(03)00210-0

De Franceschi, G., Vivattanasarn, T., Saleem, A. B., & Solomon, S. G. (2016). Vision guides selection of freeze or flight defense strategies in mice. *Current Biology*, *26*(16), 2150–2154. https://doi.org/10.1016/j.cub.2016.06.006

Deng, X., Gu, L., Sui, N., Guo, J., & Liang, J. (2019). Parvalbumin interneuron in the ventral hippocampus functions as a discriminator in social memory. *Proceedings of the National Academy of Sciences of the United States of America*, *116*(33), 16583–16592. https://doi.org/10.1073/pnas.1819133116

Dimou, L., Simon, C., Kirchhoff, F., Takebayashi, H., & Gotz, M. (2008). Progeny of Olig2-expressing progenitors in the gray and white matter of the adult mouse cerebral cortex. *Journal of Neuroscience*, *28*(41), 10434–10442. https://doi.org/10.1523/JNEUROSCI.2831-08.2008

Dubey, M., Pascual-Garcia, M., Helmes, K., Wever, D. D., Hamada, M. S., Kushner, S. A., & Kole, M. H. P. (2022). Myelination synchronizes cortical oscillations by consolidating parvalbumin-mediated phasic inhibition. *eLife*, *11*, e73827. https://doi.org/10.7554/eLife.73827

Eichenbaum, H. (2017). Prefrontal–hippocampal interactions in episodic memory. *Nature Reviews. Neuroscience*, *18*(9), 547–558. https://doi.org/10.1038/nrn.2017.74

El Waly, B., Cayre, M., & Durbec, P. (2018). Promoting myelin repair through in vivo neuroblast reprogramming. *Stem Cell Reports*, *10*(5), 1492–1504. https://doi.org/10.1016/j.stemcr.2018.02.015

Ennaceur, A., & Delacour, J. (1988). A new one-trial test for neurobiological studies of memory in rats. 1: Behavioral data. *Behavioural Brain Research*, *31*(1), 47–59. https://doi.org/10.1016/0166-4328(88)90157-X

Etxeberria, A., Hokanson, K. C., Dao, D. Q., Mayoral, S. R., Mei, F., Redmond, S. A., Ullian, E. M., & Chan, J. R. (2016). Dynamic modulation of myelination in response to visual stimuli alters optic nerve conduction velocity. *Journal of Neuroscience*, *36*(26), 6937–6948. https://doi.org/10.1523/JNEUROSCI.0908-16.2016

Eugenin von Bernhardi, J., & Dimou, L. (2022). Oligodendrogenesis is a key process for cognitive performance improvement induced by voluntary physical activity. *Glia*, *70*(6), 1052–1067. https://doi.org/10.1002/glia.24155

Ferraris, M., Ghestem, A., Vicente, A. F., Nallet-Khosrofian, L., Bernard, C., & Quilichini, P. P. (2018). The nucleus Reuniens controls long-range Hippocampo–prefrontal gamma synchronization during slow oscillations. *The Journal of Neuroscience*, *38*(12), 3026–3038. https://doi.org/10.1523/JNEUROSCI.3058-17.2018

Franco-Pons, N., Torrente, M., Colomina, M. T., & Vilella, E. (2007). Behavioral deficits in the cuprizone-induced murine model of

demyelination/remyelination. *Toxicology Letters*, *169*(3), 205–213. https://doi.org/10.1016/j.toxlet.2007.01.010

Fries, P. (2015). Rhythms for cognition: communication through coherence. *Neuron*, *88*(1), 220–235. https://doi.org/10.1016/j.neuron.2015.09.034

Galarreta, M., & Hestrin, S. (2002). Electrical and chemical synapses among parvalbumin fast-spiking GABAergic interneurons in adult mouse neocortex. *Proceedings of the National Academy of Sciences of the United States of America*, *99*(19), 12438–12443. https://doi.org/10.1073/pnas.192159599

Gibson, E. M., Purger, D., Mount, C. W., Goldstein, A. K., Lin, G. L., Wood, L. S., Inema, I., Miller, S. E., Bieri, G., Zuchero, J. B., Barres, B. A., Woo, P. J., Vogel, H., & Monje, M. (2014). Neuronal activity promotes Oligodendrogenesis and adaptive myelination in the mammalian brain. *Science*, *344*(6183), 1252304. https://doi.org/10.1126/science.1252304

Gil-Bea, F. J., Aisa, B., Schliebs, R., & Ramírez, M. J. (2007). Increase of locomotor activity underlying the behavioral disinhibition in tg2576 mice. *Behavioral Neuroscience*, *121*(2), 340–344. https://doi.org/10.1037/0735-7044.121.2.340

Gudi, V., Moharregh-Khiabani, D., Skripuletz, T., Koutsoudaki, P. N., Kotsiari, A., Skuljec, J., Trebst, C., & Stangel, M. (2009). Regional differences between grey and white matter in cuprizone induced demyelination. *Brain Research*, *1283*, 127–138. https://doi.org/10.1016/j.brainres.2009.06.005

Guise, K. G., & Shapiro, M. L. (2017). Medial prefrontal cortex reduces memory interference by modifying hippocampal encoding. *Neuron*, *94*(1), 183–192.e8. https://doi.org/10.1016/j.neuron.2017.03.011

Harris, J. J., & Attwell, D. (2012). The energetics of CNS white matter. *The Journal of Neuroscience*, *32*(1), 356–371. https://doi.org/10.1523/JNEUROSCI.3430-11.2012

Hazan, L., Zugaro, M., & Buzsáki, G. (2006). Klusters, NeuroScope, NDManager: A free software suite for neurophysiological data processing and visualization. *Journal of Neuroscience Methods*, *155*(2), 207–216. https://doi.org/10.1016/j.jneumeth.2006.01.017

Hinman, J. D., Peters, A., Cabral, H., Rosene, D. L., Hollander, W., Rasband, M. N., & Abraham, C. R. (2006). Age-related molecular reorganization at the node of Ranvier. *The Journal of Comparative Neurology*, *495*(4), 351–362. https://doi.org/10.1002/cne.20886

Ho, J., Tumkaya, T., Aryal, S., Choi, H., & Claridge-Chang, A. (2019). Moving beyond *P* values: Data analysis with estimation graphics. *Nature Methods*, *16*(7), 565–566. https://doi.org/10.1038/s41592-019-0470-3

Howell, O. W., Palser, A., Polito, A., Melrose, S., Zonta, B., Scheiermann, C., Vora, A. J., Brophy, P. J., & Reynolds, R. (2006). Disruption of neurofascin localization reveals early changes preceding demyelination and remyelination in multiple sclerosis. *Brain*, *129*(Pt 12), 3173–3185. https://doi.org/10.1093/brain/awl290

Inostroza, M., Brotons-Mas, J. R., Laurent, F., Cid, E., & de la Prida, L. M. (2013). Specific impairment of "what-where-when" episodic-like memory in experimental models of temporal lobe epilepsy. *The Journal of Neuroscience*, *33*(45), 17749–17762. https://doi.org/10.1523/JNEUROSCI.0957-13.2013

Jay, T. M., & Witter, M. P. (1991). Distribution of hippocampal CA1 and subicular efferents in the prefrontal cortex of the rat studied by means of anterograde transport ofPhaseolus vulgaris-leucoagglutinin. *The Journal of Comparative Neurology*, *313*(4), 574–586. https://doi.org/10.1002/cne.903130404

Jeffries, M. A., Urbanek, K., Torres, L., Wendell, S. G., Rubio, M. E., & Fyffe-Maricich, S. L. (2016). ERK1/2 activation in preexisting oligodendrocytes of adult mice drives new myelin synthesis and enhanced CNS function. *Journal of Neuroscience.*, *36*(35), 9186–9200. https://doi.org/10.1523/JNEUROSCI.1444-16.2016

Kato, D., & Wake, H. (2021). Myelin plasticity modulates neural circuitry required for learning and behavior. *Neuroscience Research*, *167*, 11–16. https://doi.org/10.1016/j.neures.2020.12.005

Koutsoudaki, P. N., Skripuletz, T., Gudi, V., Moharregh-Khiabani, D., Hildebrandt, H., Trebst, C., & Stangel, M. (2009). Demyelination of the hippocampus is prominent in the cuprizone model. *Neuroscience Letters*, *451*(1), 83–88. https://doi.org/10.1016/j.neulet.2008.11.058

Lasiene, J., Matsui, A., Sawa, Y., Wong, F., & Horner, P. J. (2009). Age-related myelin dynamics revealed by increased oligodendrogenesis and short internodes. *Aging Cell*, *8*(2), 201–213. https://doi.org/10.1111/j.1474-9726.2009.00462.x

Lindner, M., Fokuhl, J., Linsmeier, F., Trebst, C., & Stangel, M. (2009). Chronic toxic demyelination in the central nervous system leads to axonal damage despite remyelination. *Neuroscience Letters*, *453*(2), 120–125. https://doi.org/10.1016/j.neulet.2009.02.004

Lissner, L. J., Wartchow, K. M., Toniazzo, A. P., Gonçalves, C. A., & Rodrigues, L. (2021). Object recognition and Morris water maze to detect cognitive impairment from mild hippocampal damage in rats: A reflection based on the literature and experience. *Pharmacology Biochemistry and Behavior*, *210*, 173273. https://doi.org/10.1016/j.pbb.2021.173273

Lubetzki, C., Sol-Foulon, N., & Desmazières, A. (2020). Nodes of Ranvier during development and repair in the CNS. *Nature Reviews. Neurology*, *16*(8), 426–439. https://doi.org/10.1038/s41582-020-0375-x

Maingret, N., Girardeau, G., Todorova, R., Goutierre, M., & Zugaro, M. (2016). Hippocampo-cortical coupling mediates memory consolidation during sleep. *Nature Neuroscience*, *19*(7), 959–964. https://doi.org/10.1038/nn.4304

Mann, E. O., Suckling, J. M., Hajos, N., Greenfield, S. A., & Paulsen, O. (2005). Perisomatic feedback inhibition underlies cholinergically induced fast network oscillations in the rat hippocampus in vitro. *Neuron*, *45*(1), 105–117. https://doi.org/10.1016/j.neuron.2004.12.016

Manrique-Hoyos, N., Jürgens, T., Grønborg, M., Kreutzfeldt, M., Schedensack, M., Kuhlmann, T., Schrick, C., Brück, W., Urlaub, H., Simons, M., & Merkler, D. (2012). Late motor decline after accomplished remyelination: Impact for progressive multiple sclerosis. *Annals of Neurology*, *71*(2), 227–244. https://doi.org/10.1002/ana.22681

McKenzie, I. A., Ohayon, D., Li, H., De Faria, J. P., Emery, B., Tohyama, K., & Richardson, W. D. (2014). Motor skill learning requires active central myelination. *Science*, *346*(6207), 318–322. https://doi.org/10.1126/science.1254960

Miller, E. K., & Cohen, J. D. (2001). An integrative theory of prefrontal cortex function. *Annual Review of Neuroscience*, *24*(1), 167–202. https://doi.org/10.1146/annurev.neuro.24.1.167

Mitra, P. P., & Pesaran, B. (1999). Analysis of dynamic brain imaging data. *Biophysical Journal*, *76*(2), 691–708. https://doi.org/10.1016/S0006-3495(99)77236-X

Möbius, W., Nave, K. A., & Werner, H. B. (2016). Electron microscopy of myelin: Structure preservation by high-pressure freezing. *Brain Research*, *1641*, 92–100. https://doi.org/10.1016/j.brainres.2016.02.027

Mohamed, A., Al-Kafaji, G., Almahroos, A., Almosawi, Z., Alalwan, H., Abdulla, R., Alammadi, F., Almubarak, A., Al-Mahrezi, A., & Kamal, A. (2019). Effects of enhanced environment and induced depression on cuprizone mouse model of demyelination. *Experimental and Therapeutic Medicine*, *18*(1), 566–572. https://doi.org/10.3892/etm.2019.7654

Montgomery, S. M., & Buzsáki, G. (2007). Gamma oscillations dynamically couple hippocampal CA3 and CA1 regions during memory task performance. *Proceedings of the National Academy of Sciences of the United States of America*, *104*(36), 14495–14500. https://doi.org/10.1073/pnas.0701826104

Murray, A. J., Woloszynowska-Fraser, M. U., Ansel-Bollepalli, L., Cole, K. L. H., Foggetti, A., Crouch, B., Riedel, G., & Wulff, P. (2015). Parvalbumin-positive interneurons of the prefrontal cortex support working memory and cognitive flexibility. *Scientific Reports*, *5*(1), 16778. https://doi.org/10.1038/srep16778

Muzumdar, M. D., Tasic, B., Miyamichi, K., Li, L., & Luo, L. (2007). A global double-fluorescent Cre reporter mouse. *Genesis*, *45*(9), 593–605. https://doi.org/10.1002/dvg.20335

Nickel, M., & Gu, C. (2018). Regulation of central nervous system myelination in higher brain functions. *Neural Plasticity*, *2018*, 1–12. https://doi.org/10.1155/2018/6436453

Noori, R., Park, D., Griffiths, J. D., Bells, S., Frankland, P. W., Mabbott, D., & Lefebvre, J. (2020). Activity-dependent myelination: A glial mechanism of oscillatory self-organization in large-scale brain networks. *Proceedings of the National Academy of Sciences of the United States of America*, *117*(24), 13227–13237. https://doi.org/10.1073/pnas.1916646117

Nyamoya, S., Steinle, J., Chrzanowski, U., Kaye, J., Schmitz, C., Beyer, C., & Kipp, M. (2019). Laquinimod supports remyelination in non-supportive environments. *Cell*, *8*(11), E1363. https://doi.org/10.3390/cells8111363

Omotoso, G. O., Gbadamosi, I. T., Afolabi, T. T., Abdulwahab, A. B., & Akinlolu, A. A. (2018). Ameliorative effects of *Moringa* on cuprizone-induced memory decline in rat model of multiple sclerosis. *Anatomy & Cell Biology*, *51*(2), 119–127. https://doi.org/10.5115/acb.2018.51.2.119

Orthmann-Murphy, J., Call, C. L., Molina-Castro, G. C., Hsieh, Y. C., Rasband, M. N., Calabresi, P. A., & Bergles, D. E. (2020). Remyelination alters the pattern of myelin in the cerebral cortex. *eLife*, *9*, e56621. https://doi.org/10.7554/eLife.56621

Pajevic, S., Basser, P. J., & Fields, R. D. (2014). Role of myelin plasticity in oscillations and synchrony of neuronal activity. *Neuroscience*, *276*, 135–147. https://doi.org/10.1016/j.neuroscience.2013.11.007

Pan, S., Mayoral, S. R., Choi, H. S., Chan, J. R., & Kheirbek, M. A. (2020). Preservation of a remote fear memory requires new myelin formation. *Nature Neuroscience*, *23*(4), 487–499. https://doi.org/10.1038/s41593-019-0582-1

Patrikios, P., Stadelmann, C., Kutzelnigg, A., Rauschka, H., Schmidbauer, M., Laursen, H., Sorensen, P. S., Bruck, W., Lucchinetti, C., & Lassmann, H. (2006). Remyelination is extensive in a subset of multiple sclerosis patients. *Brain*, *129*(12), 3165–3172. https://doi.org/10.1093/brain/awl217

Peng, X., & Burwell, R. D. (2021). Beyond the hippocampus: The role of parahippocampal-prefrontal communication in context-modulated behavior. *Neurobiology of Learning and Memory*, *185*, 107520. https://doi.org/10.1016/j.nlm.2021.107520

Pfeiffer, F., Frommer-Kaestle, G., & Fallier-Becker, P. (2019). Structural adaption of axons during de- and remyelination in the cuprizone mouse model. *Brain Pathology*, *29*(5), 675–692. https://doi.org/10.1111/bpa.12748

Phillips, M. L., Robinson, H. A., & Pozzo-Miller, L. (2019). Ventral hippocampal projections to the medial prefrontal cortex regulate social memory. *eLife*, *8*, e44182. https://doi.org/10.7554/eLife.44182

Quilichini, P., Sirota, A., & Buzsáki, G. (2010). Intrinsic circuit organization and theta-gamma oscillation dynamics in the entorhinal cortex of the rat. *The Journal of Neuroscience*, *30*(33), 11128–11142. https://doi.org/10.1523/JNEUROSCI.1327-10.2010

Ragozzino, M. E., Detrick, S., & Kesner, R. P. (1999). Involvement of the prelimbic-infralimbic areas of the rodent prefrontal cortex in behavioral flexibility for place and response learning. *The Journal of Neuroscience*, *19*(11), 4585–4594.

Ragozzino, M. E., Kim, J., Hassert, D., Minniti, N., & Kiang, C. (2003). The contribution of the rat prelimbic-infralimbic areas to different forms of task switching. *Behavioral Neuroscience*, *117*(5), 1054–1065. https://doi.org/10.1037/0735-7044.117.5.1054

Rivers, L. E., Young, K. M., Rizzi, M., Jamen, F., Psachoulia, K., Wade, A., Kessaris, N., & Richardson, W. D. (2008). PDGFRA/NG2 glia generate myelinating oligodendrocytes and piriform projection neurons in adult mice. *Nature Neuroscience*, *11*(12), 1392–1401. https://doi.org/10.1038/nn.2220

Sen, M. K., Mahns, D. A., Coorssen, J. R., & Shortland, P. J. (2019). Behavioural phenotypes in the cuprizone model of central nervous system demyelination. *Neuroscience & Biobehavioral Reviews*, *107*, 23–46. https://doi.org/10.1016/j.neubiorev.2019.08.008

Shimizu, T., Nayar, S. G., Swire, M., Jiang, Y., Grist, M., Kaller, M., Sampaio Baptista, C., Bannerman, D. M., Johansen-Berg, H., Ogasawara, K., Tohyama, K., Li, H., & Richardson, W. D. (2023). Oligodendrocyte dynamics dictate cognitive performance outcomes of working memory training in mice. *Nature Communications*, *14*(1), 6499. https://doi.org/10.1038/s41467-023-42293-4

Spellman, T., Rigotti, M., Ahmari, S. E., Fusi, S., Gogos, J. A., & Gordon, J. A. (2015). Hippocampal–prefrontal input supports spatial encoding in working memory. *Nature*, *522*(7556), 309–314. https://doi.org/10.1038/nature14445

Steadman, P. E., Xia, F., Ahmed, M., Mocle, A. J., Penning, A. R. A., Geraghty, A. C., Steenland, H. W., Monje, M., Josselyn, S. A., & Frankland, P. W. (2020). Disruption of Oligodendrogenesis impairs memory consolidation in adult mice. *Neuron*, *105*(1), 150–164.e6. https://doi.org/10.1016/j.neuron.2019.10.013

Szabo, G. G., Farrell, J. S., Dudok, B., Hou, W. H., Ortiz, A. L., Varga, C., Moolchand, P., Gulsever, C. I., Gschwind, T., Dimidschstein, J., Capogna, M., & Soltesz, I. (2022). Ripple-selective GABAergic projection cells in the hippocampus. *Neuron*, *110*(12), 1959–1977.e9. https://doi.org/10.1016/j.neuron.2022.04.002

Todorova, R., & Zugaro, M. (2018). Hippocampal ripples as a mode of communication with cortical and subcortical areas. *Hippocampus*, *30*(1), 39–49. https://doi.org/10.1002/hipo.22997

Tomas-Roig, J., Torrente, M., Cabré, M., Vilella, E., & Colomina, M. T. (2019). Long lasting behavioural effects on cuprizone fed mice after neurotoxicant withdrawal. *Behavioural Brain Research*, *363*, 38–44. https://doi.org/10.1016/j.bbr.2019.01.036

Traub, R. D., Whittington, M. A., Gutiérrez, R., & Draguhn, A. (2018). Electrical coupling between hippocampal neurons: Contrasting roles of principal cell gap junctions and interneuron gap junctions. *Cell and Tissue Research*, *373*(3), 671–691. https://doi.org/10.1007/s00441-018-2881-3

Verret, L., Krezymon, A., Halley, H., Trouche, S., Zerwas, M., Lazouret, M., Lassalle, J. M., & Rampon, C. (2013). Transient enriched housing before amyloidosis onset sustains cognitive improvement in Tg2576 mice. *Neurobiology of Aging*, *34*(1), 211–225. https://doi.org/10.1016/j.neurobiolaging.2012.05.013

Wang, X. J., & Buzsáki, G. (1996). Gamma oscillation by synaptic inhibition in a hippocampal interneuronal network model. *The Journal of Neuroscience*, *16*(20), 6402–6413.

Xin, W., & Chan, J. R. (2020). Myelin plasticity: Sculpting circuits in learning and memory. *Nature Reviews. Neuroscience*, *21*(12), 682–694. https://doi.org/10.1038/s41583-020-00379-8

Xing, Y. L., Roth, P. T., Stratton, J. A. S., Danne, J., Ellis, S. L., Ng, S. W., Kilpatrick, T. J., & Merson, T. D. (2014). Adult Neural Precursor Cells from the Subventricular Zone Contribute Significantly to Oligodendrocyte Regeneration and Remyelination. *The Journal Of Neuroscience*, *19*, 14128–46.

Yamamoto, J., Suh, J., Takeuchi, D., & Tonegawa, S. (2014). Successful execution of working memory linked to synchronized high-frequency gamma oscillations. *Cell*, *157*(4), 845–857. https://doi.org/10.1016/j.cell.2014.04.009

Yoon, T., Okada, J., Jung, M. W., & Kim, J. J. (2008). Prefrontal cortex and hippocampus subserve different components of working memory in rats. *Learning & Memory*, *15*(3), 97–105. https://doi.org/10.1101/lm.850808

Young, K. M., Psachoulia, K., Tripathi, R. B., Dunn, S. J., Cossell, L., Attwell, D., Tohyama, K., & Richardson, W. D. (2013). Oligodendrocyte dynamics in the healthy adult CNS: Evidence for myelin remodeling.

Neuron, *77*(5), 873–885. https://doi.org/10.1016/j.neuron.2013.01.006

Zaimi, A., Wabartha, M., Herman, V., Antonsanti, P. L., Perone, C. S., & Cohen-Adad, J. (2018). AxonDeepSeg: Automatic axon and myelin segmentation from microscopy data using convolutional neural networks. *Scientific Reports*, *8*(1), 3816. https://doi.org/10.1038/s41598-018-22181-4

Zawadzka, M., Rivers, L. E., Fancy, S. P. J., Zhao, C., Tripathi, R., Jamen, F., Young, K., Goncharevich, A., Pohl, H., Rizzi, M., Rowitch, D. H., Kessaris, N., Suter, U., Richardson, W. D., & Franklin, R. J. M. (2010). CNS-resident glial progenitor/stem cells produce Schwann cells as well as oligodendrocytes during repair of CNS demyelination. *Cell Stem Cell*, *6*(6), 578–590. https://doi.org/10.1016/j.stem.2010.04.002

SUPPORTING INFORMATION

Additional supporting information can be found online in the Supporting Information section at the end of this article.

How to cite this article: Mercier, O., Quilichini, P. P., Magalon, K., Gil, F., Ghestem, A., Richard, F., Boudier, T., Cayre, M., & Durbec, P. (2024). Transient demyelination causes long-term cognitive impairment, myelin alteration and network synchrony defects. *Glia*, 1–22. https://doi.org/10.1002/glia.24513